Design and Optimization of an AFM Probe Based on Piezoresistance Effect

Mehran Hosseini

A Thesis

in

The Department

of

Electrical and Computer Engineering

Presented in Partial Fulfillment of the Requirements
for the Degree of Master of Applied Science (Electrical Engineering) at
Concordia University
Montreal, Quebec, Canada

April 2005

Your file Votre référence
ISBN: 0-494-04377-6
Our file Notre référence
ISBN: 0-494-04377-6

ABSTRACT

Design and Optimization of an AFM Probe Based on Piezoresistance Effect

Mehran Hosseini

Atomic Force Microscopy (AFM) probes with embedded stress sensors have demonstrated the ability to address key issues such as simplicity, reliability, and responsiveness to parallel scanning techniques and therefore are promising devices for AFM applications. Even though there are some other candidates for integration as sensor parts with the mechanical structure of the device (e.g. MOS transistors), piezoresistive materials are still among the most attractive sensors used in cantilever-based devices.

Standard CMOS fabrication process is a suitable technology, which allows integration of sensor, mechanical parts and electronic signal conditioning/processing circuits on the same chip.

In this thesis we present design and optimization of an AFM probe with integrated polysilicon piezoresistive sensor, based on MEMS techniques. Design goal is to optimize a combination of sensitivity and signal-to-noise (S/N) ratio to achieve the minimum lower detection limit, while maintaining the other important factors such as eigenfrequencies, in an acceptable range.

Standard CMOS 0.35μm technology is considered as the target fabrication process as well as a multistage masked post-CMOS micro-machining process to release the structure. A sophisticated geometry of the cantilever and the sensor, along with the optimized length of sensor branches in terms of S/N ratio is achieved.

ACKNOWLEDGMENTS

I would like to express my sincere gratitude to my supervisors, Dr. Mojtaba Kahrizi and Dr. Victor Rossokhaty, for their support over the past two years. Their knowledge, their enlightenment and encouragement as well as their invaluable instructions, helped me to a great extent, and made this thesis possible.

Also I wish to express my truly appreciation to the faculty of Engineering and Computer Science at Concordia University, my schoolmates and my friends, for their helps and their information sharing.

Furthermore I would like to thank Canadian Microelectronics Corporation (CMC) for their technical assistances and National Sciences and Engineering Research Council of Canada (NSERC) for their financial supports.

Finally and most importantly, I wish to greatly thank my dear wife, Leila and my kind parents, for all of their encouragement, their patience and their endless devotion.

TABLE OF CONTENTS

LIST OF FIGURES

LIST OF TABLES

THESIS OVERVIEW

The first chapter covers the basic concepts, including the general description of AFM. Different modes of AFM, as well as its applications and the explanations of the various systems based on this technique, are also given in this chapter. The related measurement issues along with the target fabrication technology are discussed in this chapter as well.

Chapter 2 includes the mathematical and physical explanations of some important phenomena, which are necessary for design and analysis of the proposed probe structure.

The structure of the proposed probe, followed by a discussion about the target post-processing steps, is presented in Chapter 3. This chapter also contains the modeling results of the design, which characterizes the mechanical and electrical aspects of the probe. Optimization of the recommended design in terms of S/N ratio and eigenfrequency are also covered in Chapter 3. The conclusion and the key achievements are highlighted in Chapter 4, along with some recommendations for future works.

CHAPTER 1 BASIC CONCEPTS

1.1 General Description of AFM

1.1.1 Introduction

Although Atomic Force Microscopy is the most well known application of micro cantilevers constructed using MEMS techniques, these cantilevers have been proposed for a variety of applications, including the measurement of topography [1,2] - acceleration [3] - magnetic fields [4] - acoustic [5] - stress [6] - humidity [7] - physical/mechanical properties and fabrication variables in the material sciences [8,9] - magnetic polarization, embedded electric charge [10] - capacitance, and electrical resistance [11] - Phenomena such as abrasion, adhesion, cleaning, corrosion, etching, lubrication, plating, polishing and friction [12] as well as application such as data storage [13] and biological applications like: investigation of DNA, proteins, and cells in biological studies [14] - structure and component distribution in polymer science[15] and Pharmaceutical research [16].

The common functional principle of almost all these applications is to measure deflection of a cantilever as a function of a particular quantity. Sensing mechanism plays a crucial role in terms of determining the main characteristics of the sensor such as sensitivity, signal to noise ratio and stability, as well as the application aspects like responsiveness to parallelism, and sensor components integrated in systems-on-chip have shown appreciable performance in a majority of these respects.

AFM is a powerful tool for the investigation of morphologies and mechanical properties of surfaces. The major achievement of AFM lies in its ability to measure tiny

forces acting between a sharp tip and a sample. Even atomic and molecular resolution can now be obtained using dynamic modes of operation. This technique was developed mainly to image the surface of materials in atomic resolution and now it is being used to solve processing and materials problems in a wide range of technologies.

There are some other competitors for AFM, like STM (Scanning Tunneling Microscopy), SEM (Scanning Electron Microscopy), TEM (Transmission Electron Microscopy) as well as Optical Microscopy. While there are advantages and disadvantages for each of these methods, AFM has been proved to be a very efficient method compared to its competitors.

AFM belongs to a general family of techniques called scanning probe microscopy (SPM). SPM began with the development of the first scanning tunneling microscope (STM) at IBM laboratories in Zurich in 1982. The capabilities of STM to resolve the atomic structures of different materials resulted in the Nobel Prize for its inventors in1986. The application of STM is restricted to conductor or semiconductor materials, but AFM is an extensive method that makes the study of any kind of solids (including insulators) possible. The first AFM was made by meticulously gluing a tiny shard of diamond onto one end of a tiny strip of gold foil. In the fall of 1985 Gerd Binnig and Christopher Gerber used the cantilever to examine insulating surfaces. A small hook at the end of the cantilever was pressed against the surface while the sample was scanned beneath the tip. The force between tip and sample was measured by tracking the deflection of the cantilever. They could delineate lateral features as small as 300 Å. And a more complete AFM system was developed in collaboration between IBM and Stanford University in 1986 [17].

AFM has been used routinely in many scientific and industrial fields in the past two decades. Today the tip-cantilever assembly typically is micro-fabricated from Polycrystalline Silicon, Silicon or Si_3N_4 and the resolution is in atomic scale (1Å). Natural frequencies of the probe up to 6 MHz [18] and a minimum detectable cantilever deflection equal to 0.3 Å [19] are some examples of the today AFM probes characteristics.

Fig.1.1 shows an AFM image of a silicon sample surface cut in (111) plane.

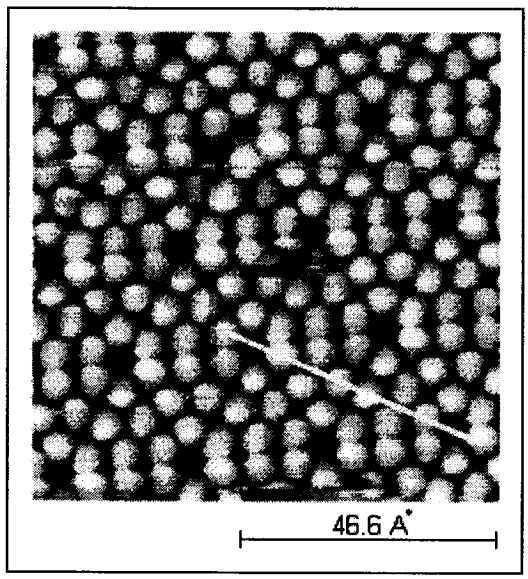

Fig.1.1.AFM image of a silicon sample cut in (111) plane

1.1.2 Interaction of the Cantilever Tip and the Sample Surface

AFM is based on the attraction and repulsion forces that exist between the atoms at the tip of the cantilever and the atoms at the surface of the sample under investigation (Fig.1.2 (b)). The tips typically have an end radius of 5 nm to 10 nm. Fig.1.2 (a) shows a diagram of the inter-atomic force versus the distance from the tip to the sample [20]. As the distance decreases, the attraction force (negative) increases, up to a point in which the

attraction force is the maximum. Further decrease in distance reverses the force direction and makes it repulsive. Negative distances in the figure happen when the tip passes the sample surface and goes deeper.

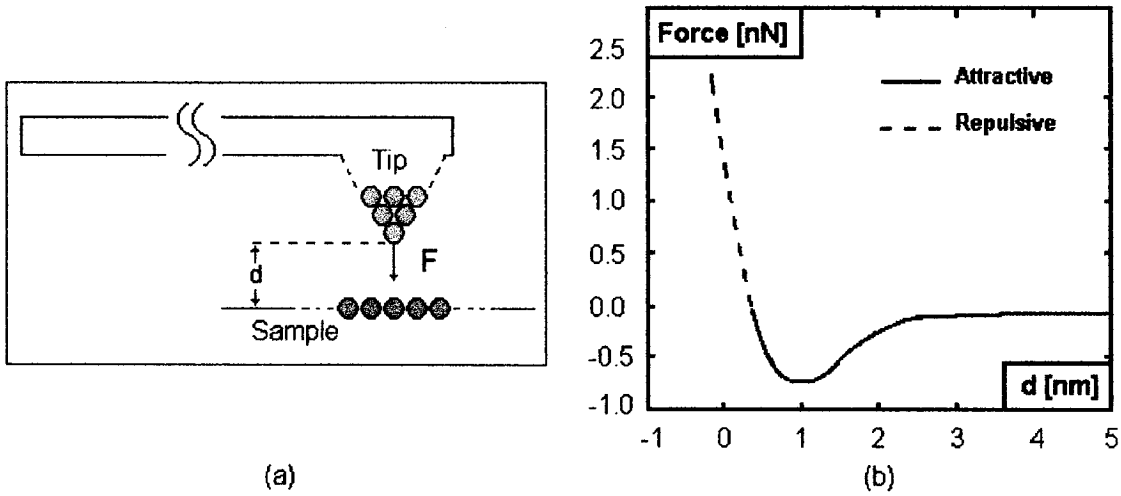

Fig.1.2. (a) Interaction between the Tip of the AFM probe and the sample (b)Attractive and repulsive forces between the tip and the sample surface, versus distance

According to the interaction of the cantilever tip and the sample surface, AFM can be classified as: Contact mode, Non-contact mode and Tapping mode.

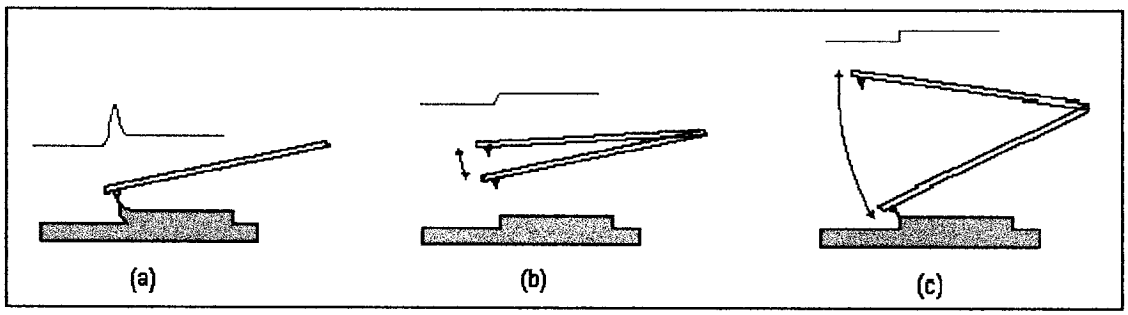

Fig.1.3. Interaction of the cantilever tip and the sample surface: (a) Contact Mode (b) Non-contact Mode (c) Tapping Mode.

1.1.2.1 Contact Mode

The contact mode where the tip scans the sample in close contact with the surface is the common mode used in the force microscope (Fig.1.3 (a)). The force on the tip is repulsive with a mean value of 10^{-8} N. This force is set by pushing the cantilever against the sample surface with some kinds of positioning mechanism. In contact mode AFM the deflection of the cantilever is sensed and compared to some desired value of deflection. If the measured deflection is different from the desired value, the feedback control system applies a voltage to the positioning mechanism to raise or lower the sample relative to the cantilever to restore the desired value of deflection. The voltage that the feedback control system applies to the positioning mechanism is a measure of the height of features on the sample surface. It is displayed as a function of the lateral position of the sample.

1.1.2.2 Non-contact Mode

The non-contact mode is used in situations where tip contact might alter the sample in subtle ways. In this mode the tip hovers 50 - 150 Angstrom above the sample surface (Fig.1.3 (b)). Attractive Van der Waals forces acting between the tip and the sample are detected, and topographic images are constructed by scanning the tip above the surface. Unfortunately the attractive forces from the sample are substantially weaker than the forces used by contact mode. Therefore the tip must be given a small oscillation so that AC detection methods can be used to detect the small forces between the tip and the sample by measuring the change in amplitude, phase, or frequency of the oscillating cantilever in response to force gradients from the sample.

1.1.2.3 Tapping Mode

Tapping mode is a key advance in AFM. Tapping mode overcomes problems associated with friction, adhesion, electrostatic forces, and other difficulties by alternatively placing the tip in contact with the surface to provide high resolution and then lifting the tip off the surface to avoid dragging the tip across the surface (Fig.1.3 (c)). Tapping mode imaging is implemented in ambient air by oscillating the cantilever assembly at or near the cantilever's resonant frequency using a piezoelectric crystal. The piezo motion causes the cantilever to oscillate with a high amplitude (typically greater than 20nm) when the tip is not in contact with the surface. The oscillating tip is then moved toward the surface until it begins to lightly touch, or tap the surface. During scanning, the vertically oscillating tip alternately contacts the surface and lifts off, generally at a frequency of 50 to 500 kHz . As the oscillating cantilever begins to intermittently contact the surface, the cantilever oscillation is necessarily reduced due to energy loss caused by the tip contacting the surface. The reduction in oscillation amplitude is used to identify and measure surface features.

During tapping mode operation, the cantilever oscillation amplitude is maintained constant by a feedback loop.

Tapping mode inherently prevents the tip from sticking to the surface and causing damage during scanning. Unlike contact and non-contact modes, when the tip contacts the surface, it has sufficient oscillation amplitude to overcome the tip-sample adhesion forces. Also, the surface material is not pulled sideways by shear forces since the applied force is always vertical. Another advantage of the tapping mode technique is its large,

linear operating range. This makes the vertical feedback system highly stable, allowing routine reproducible sample measurements.

1.1.2.4 Comparison of Three Methods

In contact AFM electrostatic and/or surface tension forces pull the scanning tip toward the surface. Contact mode imaging is heavily influenced by frictional and adhesive forces compared to non-contact or tapping mode.

Non-contact imaging generally provides low resolution and can also be hampered by the contaminant layer, which can interfere with oscillation.

Tapping mode AFM was developed as a method to achieve high resolution without inducing destructive frictional forces both in air and fluid. With the tapping mode technique, the very soft and fragile samples can be imaged successfully. Also, incorporated with *Phase Imaging* (described below), the tapping mode AFM can be used to analyze the components of the sample.

1.1.3 Phase Imaging

Phase Imaging is a powerful extension of Tapping Mode AFM that provides nanometer-scale information about surface structure often not revealed by other SPM techniques. By mapping the phase of the cantilever oscillation during the tapping mode scanning, phase imaging goes beyond simple topographical mapping to detect variations in composition, adhesion, friction, viscoelasticity, and perhaps other properties. Applications include identification of contaminants, mapping of different components in composite materials, and differentiating regions of high and low surface adhesion or hardness.

1.1.4 Force Curve Measurements

In addition to these topographic measurements, the AFM can also provide much more information. The AFM can also record the amount of force felt by the cantilever as the probe tip is brought close to - and even indented into - a sample surface and then pulled away. This technique can be used to measure the long range attractive or repulsive forces between the probe tip and the sample surface, elucidating local chemical and mechanical properties like adhesion and elasticity, and even thickness of molecular layers or bond rupture lengths.

Force curves (force-versus-distance curve) typically show the deflection of the free end of the AFM cantilever as the fixed end of the cantilever is brought vertically towards and then away from the sample surface.

1.1.5 AFM Resolution

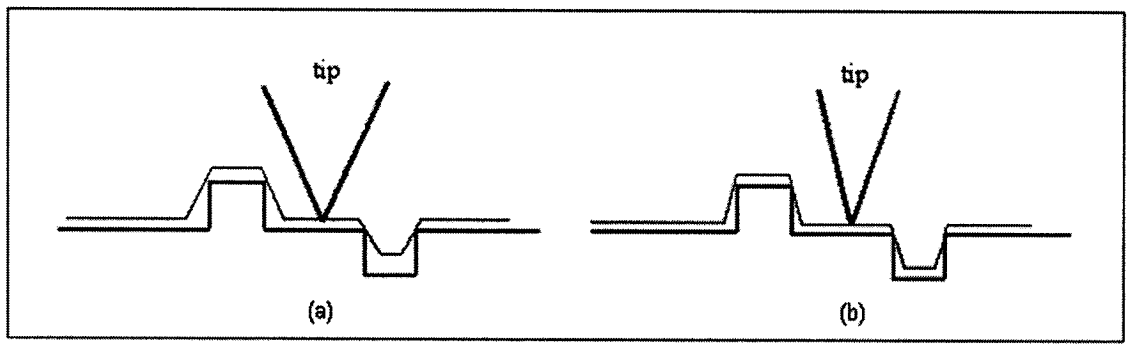

Fig.1.4. The effect of related sizes of tip and sample roughness, on the output signal

The concept of resolution in AFM is different from radiation-based microscopy, because AFM imaging is a three-dimensional imaging technique. The ability to distinguish two separate points on an image is the standard by which lateral resolution is usually defined. There is clearly an important distinction between images resolved by

wave optics and scanning probe techniques. The former is limited by diffraction, and later primarily by probe geometry and sample geometry. Lateral resolution in the range of 1 is t ypical for AFM probes [22].

1.1.6 Various Designs of Cantilevers

Depending on the application, various designs of cantilever and tip are possible. Also Actuation mechanism can be based on various physical forces and can be integrated into or separated from cantilever structure. Fig.1.5 shows two possible designs for AFM probes.

The micro-cantilevers designed for SPM applications typically have dimensions in the 100 microns range and their resonance frequencies are in the 10–300 kHz range [23].

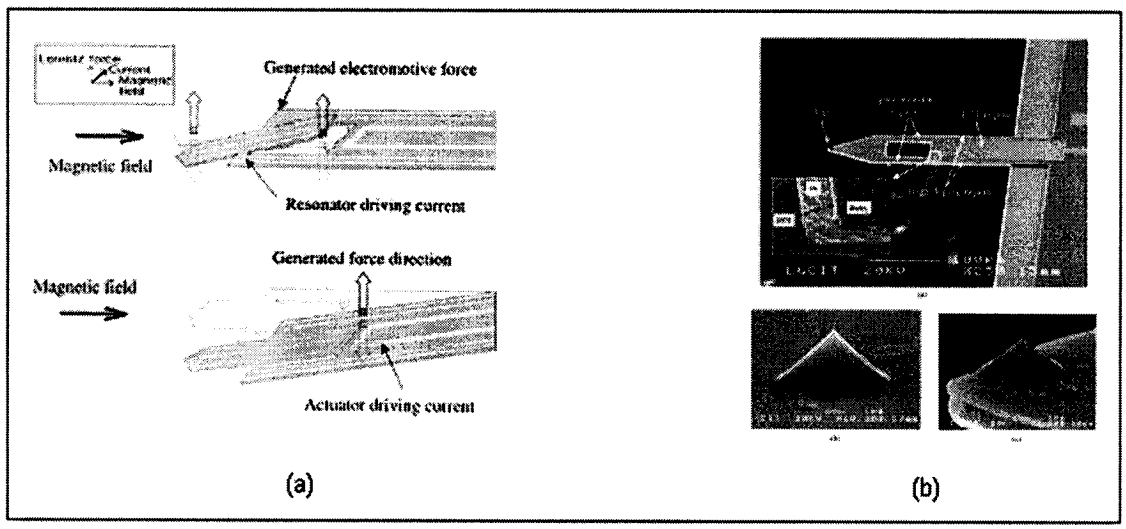

Fig.1.5. (a) A cantilever in which, tip has a separate movement related to cantilever and this movement is provided by electromagnetic force[24] (b) A cantilever that has a fixed tip and cantilever movement is caused by PZT actuator[25].

1.1.7 Various Measurement Methods

The force between the tip and the sample surface is very small therefore the detection system usually measures the force by sensing the deflection of the cantilever. Detecting micro-movements of the cantilever can be done in several ways and depending on the method and technology, measurement devices may be integrated or separated from cantilever frame. Fig.1.6 (a) shows a system in which the deflection of the cantilever is changed to the deviation of a laser beam from its original path. The movement of the beam then is detected by photo-detectors and is used for both the deflection measurement and for adjusting the vertical position of the cantilever [26,27]. Displacement of the order of 0.1 nm can be measured using optical beam deflection [23].

In Fig.1.6 (b) the sensor part (a piezoresistor) is integrated inside the structure of the cantilever and a Wheatstone bridge has been used to measure the change in the resistance of the sensor due to stress, which is in turn a function of the applied force to the tip. Fig.1.6 (b) also shows the feedback mechanism used to change the position of the cantilever via a PZT actuator. The systems based on laser beam deviation are more complex than those based on integrated sensors.

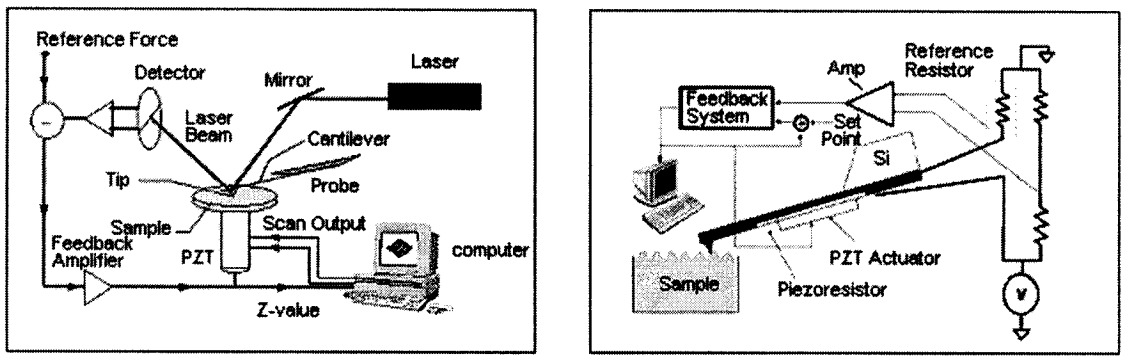

(a) (b)

Fig.1.6. (a) Cantilever deflection detection by Laser beam (b) Using integrated stress sensors as tension detectors[28].

Also they face some calibration difficulties and applying parallel techniques (using several parallel probes at the same time) is not simple in these systems. On the other hand measurement systems that use integrated sensors are much simpler and are very susceptible to parallelism. In our design we have chosen integrated piezoresistor sensing, regardless of any specific method of actuation.

1.1.8 Important Factors in AFM System Design

In designing a complete AFM system there are several important factors that should be taken into account, among them: sensitivity, resolution, speed, noise effect, power dissipation, simplicity of manufacturing, having the least effect on the sample, type of extracted information, geometric dimensions, interaction method of the cantilever (tip) and the sample, Integrating or separating of actuation mechanism to/from cantilever structure, sensing method: electronic- electromagnetic- optic etc., measurement technique: differential or simple, and integrating or separating of signal conditioning circuit to/from the same chip of cantilever structure.

Fortunately, optimization of some of these factors, act on the same direction as of the others and leads to optimization or at least improvement in other factor(s). For example, reducing cantilever dimensions could result in lower power dissipation and higher speed due to higher resonance frequency. But, It is not the case in all situations and sometimes there is a trade-off between these factors. For example (as we will prove later) weakening of the connection point of the cantilever and its base, can increase the strain at the connection point and eventually can increase sensitivity of the system, But it will reduce the speed of the measurement due to reduction in the natural frequencies of the cantilever.

1.2 General Measurement Issues

1.2.1 Definitions

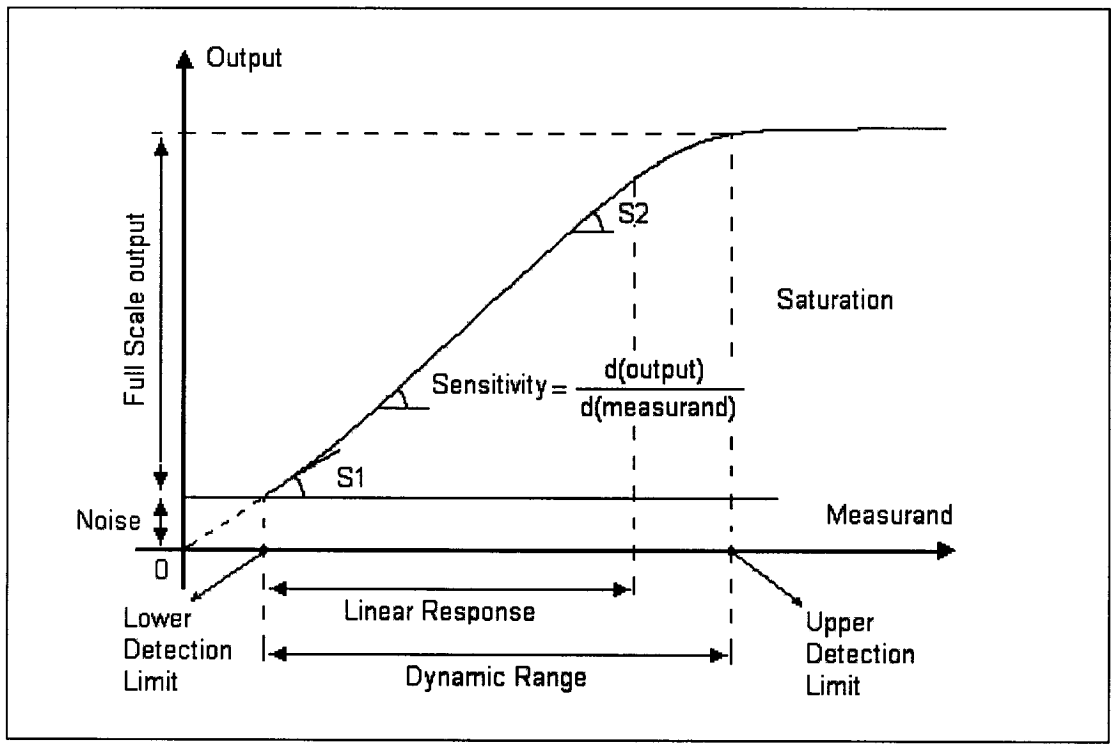

Fig.1.7. General measurement concepts

Fig.1.7 shows the general concepts of any measurement system using sensors. A sensor is defined as a device that can detect an input signal (or energy) and convert it to an appropriate output signal (or energy) (usually electric energy).

Sensitivity of a sensor is defined as:

$$Sensitivity = \frac{d(output)}{d(measurand)} \qquad \text{(Eq.1.1)}$$

There is always a limitation in terms of the range of the input that can be measured by the sensor. For Large values of measurand there is a saturation part in the input-output relationship of the sensor that determines the *Upper detection limit* of the input. Detecting small values of the input, faces another challenge, which is different sources of noise in

the system. There is always a noise signal (coming from different sources) that is added (or subtracted) to the input signal and therefore, the measurement of input signal levels, below or comparable to this noise level is subject to a serious error. This fact sets a *Lower detection limit* to the input signal. As can be derived from Fig.1.7, this lower detection limit is a function of both, the sensitivity (the slope of the input-output curve) and the noise level. The distance between these two limits determines the *dynamic ran*ge of the sensor.

Usually there is a range inside the dynamic range, over which the sensitivity of the device can be considered almost constant, and it is called the *linear range* of the sensor (this range does not necessarily start from the lower detection limit). Linearity is defined over this range as:

$$Linearity = \frac{|S1 - S2|}{\frac{S1 + S2}{2}} \times 100\% \qquad \text{(Eq.1.2)}$$

S1 and S2 are the minimum and the maximum sensitivities over the linear range. The selected sensor for this project is a piezoresistor that is used basically as a strain gauge. Therefore in the following discussion we concentrate on piezoresistors.

1.2.2 Electronic Noise

Among different noise sources in an electronic device, i.e. thermal noise, shot noise, generation-recombination noise and *1/f* noise, the dominant contributors in the operation of a piezoresistor are thermal noise and low frequency (*1/f*) noise [56]. Thus, the electronic noise can be computed using the power spectral densities of thermal noise and low frequency noise [29,30].

1.2.2.1 Thermal Noise

Voltage fluctuations, at the external terminals of a resistor, can be detected due to the scattering of electrons by the thermal vibrations of the lattice. These fluctuations are present above absolute zero temperature, in any device that dissipates energy. Since higher temperatures lead to increased vibration motion, thermal noise power spectral density (PSD) (unit V^2/Hz) is directly proportional to temperature. In addition, thermal noise PSD is independent of frequency. The thermal noise PSD (S_{TN}) is given by [53]:

$$S_{TN} = 4kTR \qquad \text{(Eq.1.3)}$$

where k is the Boltzmann constant, R is the resistance, and T is the absolute temperature. Assuming a Wheatstone bridge to be used for measuring the change in the sensor resistance (more on this later), and using a band-pass filter $[f_1 \rightarrow f_2]$ to eliminate the noise effect outside the measured signal frequency range, the rms noise voltage, $\overline{V_{TN}}$, due to thermal noise, detectable at the terminals of a Wheatstone bridge will be:

$$\overline{V_{TN}} = \sqrt{4kT\Delta fR} \qquad \text{(Eq.1.4)}$$

where $\Delta f = f_2 - f_1$ Hz

1.2.2.2 1/ f Noise

Another important noise source in piezoresistors is 1/f noise, whose PSD varies inversely with frequency when an external *dc* bias is applied. Since the PSD is more prevalent at low frequencies, it is known as low frequency noise as well. Two physical mechanisms have been proposed to describe the low frequency noise, the first is random trapping/detrapping of carriers at surface and bulk electronic traps and the second is

random mobility fluctuations. An empirical formulation for 1/f noise given by Hooge [29] will be used to model the 1/f noise in the piezoresistor. Hooge's relation for 1/f noise PSD is given by

$$S_{LFN} = \frac{\alpha_H V^2}{Nf} \qquad \text{(Eq.1.5)}$$

where α_H, known as the Hooge's parameter, is an empirically obtained constant which ranges from 5×10^{-6} to 2×10^{-3} (we use $\alpha_H = 10^{-3}$ for our design) and is sensitive to bulk crystalline silicon imperfections as well as to the interface quality, V is the applied voltage, and N is the total number of carriers. The rms noise voltage due to 1/ f noise at the terminals of a Wheatstone bridge (the same assumptions) is then:

$$\overline{V_{LFN}} = \sqrt{\frac{1}{4}\alpha_H \frac{V^2}{N} \ln\left(\frac{f_2}{f_1}\right)} \qquad \text{(Eq.1.6)}$$

Unlike the thermal noise, 1/f noise occurs under non-equilibrium conditions and is proportional to the applied voltage. From the inverse relation to the square root of the number of charge carriers, we see that 1/ f noise increases in smaller volume and higher resistivity piezoresistors (both results in smaller N).

1.2.3 Measurement Method

The sensing method in our design is based on the change of the resistance of a polysilicon piezoresistor due to stress. Although we will cover the analytical description of the following subjects later, to have a basic picture to enable us to talk about measurement method, the basic concepts and the related simple principles is presented here.

Fig.1.8 shows the deformation of a simple rectangular shape resistor under an applied axial force.

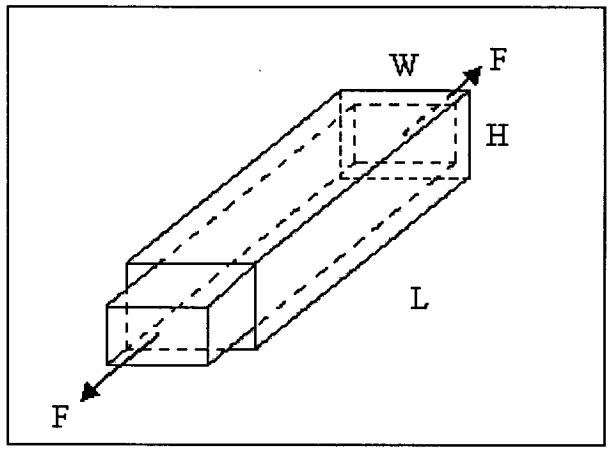

Fig.1.8. Deformation of a simple resistor due to stress

If the changes in the geometry of the resistor along L, W, and H direction are ΔL, ΔW, and ΔH respectively, to compute the change of resistance, we have:

$$R = \frac{\rho L}{A} \quad \text{and} \quad A = WH \quad \Rightarrow \quad dR = \frac{\rho}{A}dL + \frac{L}{A}d\rho - \frac{\rho L}{A^2}dA \quad \Rightarrow \quad \frac{dR}{R} = \frac{dL}{L} + \frac{d\rho}{\rho} - \frac{dA}{A}$$

As we will show later:

$$\frac{dL}{L} = \varepsilon \quad \text{and} \quad \frac{dA}{A} = \frac{dW}{W} + \frac{dH}{H} = -2v\varepsilon$$

where ε is the *strain* and v is the *Poisson's ratio* of the material of the resistor. Therefore

$$\frac{dR}{R} = (1+2v)\varepsilon + \frac{d\rho}{\rho} \qquad \text{(Eq.1.7)}$$

in this equation, the first term; $(1+2\nu)\varepsilon$ is the contribution of the geometry change of the resistor and the second term; $d\rho/\rho$ is due to piezoresistance phenomenon (more on this later).

The sensitivity of the sensor in this case is usually given by the *Gauge factor*, which is defined as the relative change in resistance, R, per unit strain, or

$$GF = \frac{dR/R}{\varepsilon} = (1+2\nu) + \frac{d\rho}{\rho\varepsilon} \qquad \text{(Eq.1.8)}$$

For metals the piezoresistance effect is negligible and since ν cannot be more than 0.5, the GF for metals is less than 2. But for silicon (mono-crystalline or poly-crystalline) depending on the direction and the structure, it can be up to 100 and even more.

A Wheatstone bridge is usually used to convert the changes in the resistance of the sensor, corresponding to a specific amount of force, to an output voltage. The circuit configuration of the bridge is shown in Fig.1.9

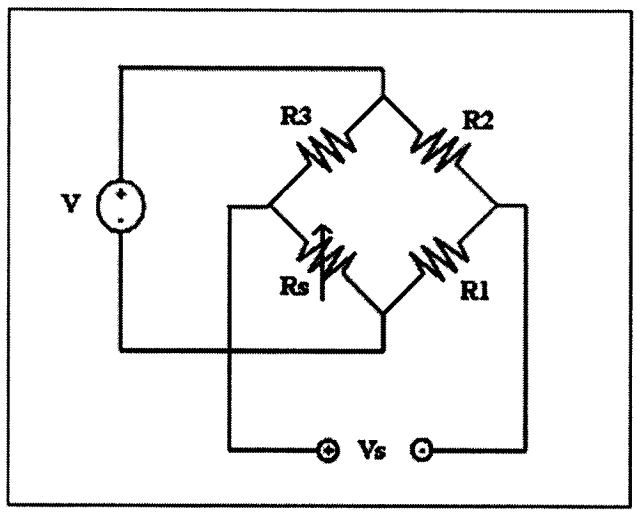

Fig .1.9. Wheatstone bridge for converting ΔRs to Voltage

Assuming that: $Rs = Rso + \Delta Rs$ where Rso is the value of the sensor resistance without the applied force and ΔRs is the change of resistance in the presence of the force, the output signal can be calculated using:

$$Vs = V\left[\frac{Rs}{(R3+Rs)} - \frac{R1}{(R2+R1)}\right]$$

To have zero output voltage in the absence of the force (called balance condition of the bridge) we should have: $\frac{R_3}{Rso} = \frac{R_2}{R_1}$ and to have the maximum output voltage for a given force, it can be shown that under the condition of $R_1 = R_2 = R_3 = Rso = R$ the output voltage is: $Vs = \frac{V}{4R} \cdot \Delta Rs$ (Eq.1.9)

In our design Rs is the resistance of the polysilicon piezoresistor, which is used as a strain gauge. In practice to enhance the sensitivity of the sensor we do not use the simple rectangular shape resistors. The conventional shape for semiconductor strain gauges is shown in Fig.1.10.

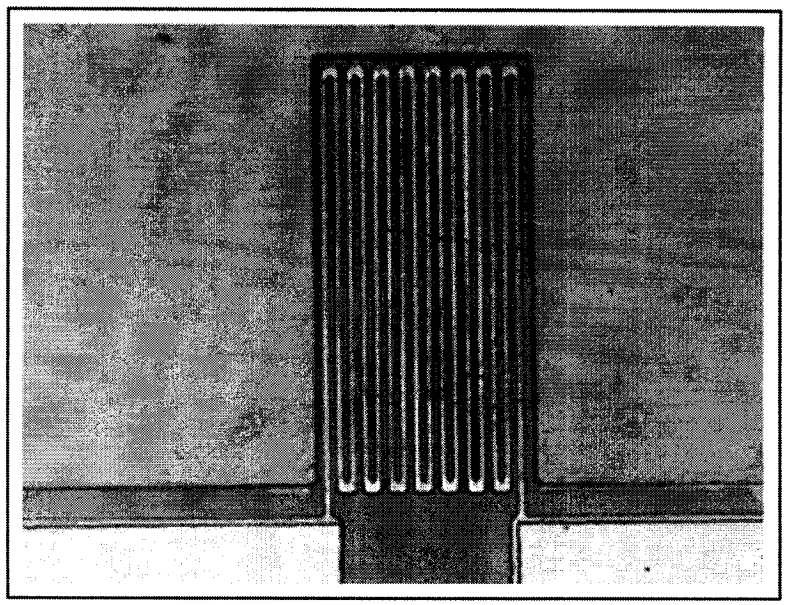

Fig.1.10. A conventional polysilicon strain gauge (meander-type resistor)[31]

Considering this method of measurement, and having the same resistances in the branches of the bridge (same material and same dimensions), along with a band-pass filter stage $[f_1 \rightarrow f_2]$, to restrict the noise power; the combined effect of thermal noise and low frequency noise, detectable as a noise voltage on Vs terminals, can be described as:

$$\overline{V_N} = \sqrt{4kT(f_2 - f_1)R + \frac{1}{4}\alpha_H \ln\left(\frac{f_2}{f_1}\right)\left(\frac{V^2}{N}\right)} \qquad \text{(Eq.1.10)}$$

1.3 Target fabrication technology

1.3.1 CMOS 0.35μm Technology

CMOS 0.35μm technology is composed of two Polysilicon layers and four Metal layers, along with insulating Oxide layers in between (Fig.1.11 (a)). The electrical connection between the layers (not shown in the figure) is possible using so called Contact and Via layers which are basically made of metals. Contacts are used to remove the Oxide layer(s) underneath each metal layer and make an electrical (as well as mechanical) connection between the desired metal layer and Poly1 or Poly2 (or substrate). Vias are used to provide connections between every two metal layers. Every MEMS device has to be built using a subset of these layers. Therefore the number, the material, the order, and the thickness of the layers are fixed for each specific technology (Like CMOS 0.35μm) and cannot be changed by a designer. The layers to be used in the structure and the geometry of different sections; are the degrees of freedom in designs to

be fabricated by standard technologies (the possibility of releasing the final structure using known post-micro-machining techniques should be taken into account).

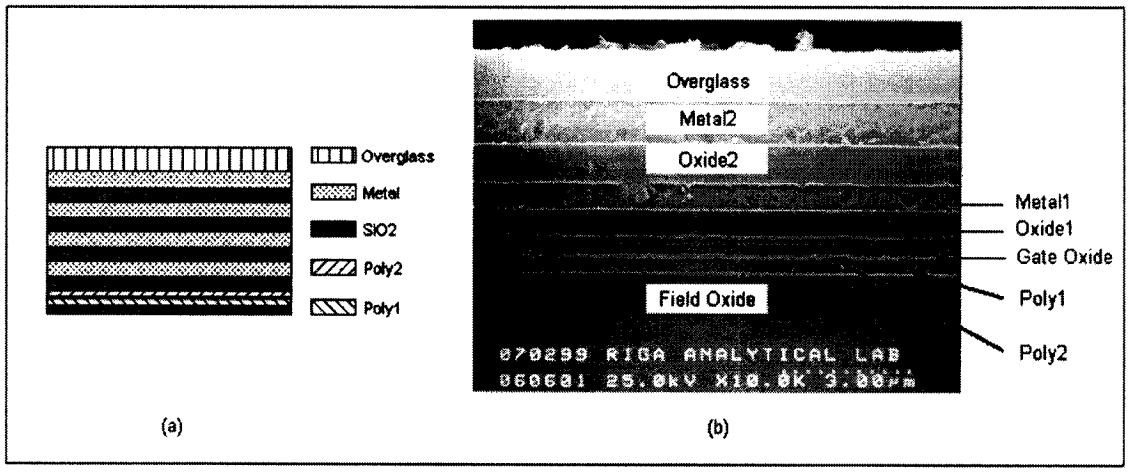

Fig.1.11. (a) schematic diagram of the different layers in CMOS 0.35μm Technology. (b) A cross section photograph of a beam fabricated using a similar CMOS technology [32].

The selection of the layers is a function of several factors. Three different groups of layers (Ploys, Oxides and Metals) have their own specific electrical and mechanical properties and based on the desired device characteristics, can be used or eliminated. Having or eliminating poly and metal layers is optional, while design rules make having the Oxide layers generally compulsory (Although they can be removed locally using Contacts and Vias). In our design, one of the most important factors that should be considered in the selection of the layers is the residual stress in the structure of the final device. The fabrication steps are performed at various temperatures (ranging from room temperature up to 1200 °C for diffusion and oxidation) and consequently thermo-mechanical stress will be induced once the chip is cooled down to room temperature. The difference between the thermal expansion of silicon, polysilicon, Oxide and metal layers is the main cause of the induced thermo-mechanical stress. Depending on the

combination of the layers, this stress (also known as residual stress) can causes (often) upward bending of the released structure (Fig.1.12).

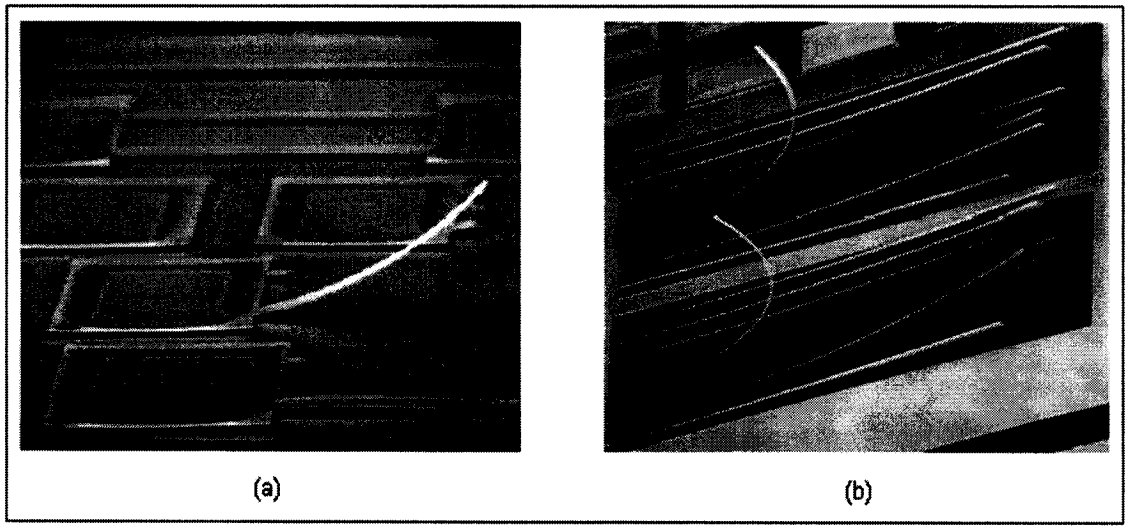

Fig.1.12. Upward bending of the released devices fabricated using CMOS technology, due to residual stress (a) [33] (b) [34]

Therefore, the combination of layers and their geometries should be in such a way that this residual stress does not alter the shape of the desired device. Thermo-mechanical stress is not the only source of stress in the fabricated structure. Dopant induced stress and stress due to oxidation volume expansion are some other sources [35].

1.3.1.1 Dopant Induced Stress

As dopants are introduced into the polysilicon layers, the mechanical state of the layers changes. The dopants may substitute for the silicon positions in the lattice. Silicon atoms are displaced forming extended defects that are lodged in the crystal lattice. Different dopants have various atomic sizes and therefore have different mechanical behavior in the crystal. Precipitates and other usually present atoms such as oxygen and carbon also alter the mechanical properties of the crystal.

1.3.1.2 Oxidation Volume Expansion

It is well known that in Silicon oxidation, the volume of Oxide is 2.2 times greater than the volume of the consumed Silicon. For planar oxidation, this presents no problem since the newly acquired volume pushes the old Oxide upward towards the unconstrained surface perpendicular to the interface. However, in non-planar regions such as in trench corners and in constrained regions such as in edges of local oxide areas, this presents a problem. For these regions, the boundaries are constrained and therefore the newly acquired Oxide volume compresses against the earlier grown Oxide. Since the Oxide has no place to move, large compressive strains build up in these regions.

1.3.2 Polycrystalline Silicon

Two of the layers in CMOS 0.35μm technology are made of Polycrystalline Silicon (Polysilicon). Polysilicon comprises small grains of single-crystal silicon separated by thin boundaries. At the grain boundaries, the grains of different orientations meet, resulting in an extremely thin amorphous layer. Due to great concentration of dangling bonds, these boundaries create potential barriers and therefore significantly influence the electrical properties of the Polysilicon layer. When the films are doped, the doping atoms can occupy these sites rendering them electrically inactive and thus affect the barrier height. This barrier is similar to Schottky barrier, through which charge carrier transport can occur in form of thermionic emission or tunneling.

The basic structure can be small random grains or columnar (Fig.1.13). These structures are highly dependent on the fabrication process and therefore it is impossible to give exact electrical and mechanical parameters that are applicable to all kind of

polysilicon layers. Values considered in our design are therefore average values reported in numerous research papers on Polysilicon. The applications for polysilicon can be traced back to the 1960s with the realization that it could be used for gates in MOS technologies to enable further reduction in dimensions. In the 1970s, it was found to be a useful material for piezoresistive applications. Since no pn junction was required, these devices could operate at higher temperatures. In the 1980s, the potential of polysilicon as a mechanical material was realized. In our design, we utilize the piezoresistance property of polysilicon to make the sensor part.

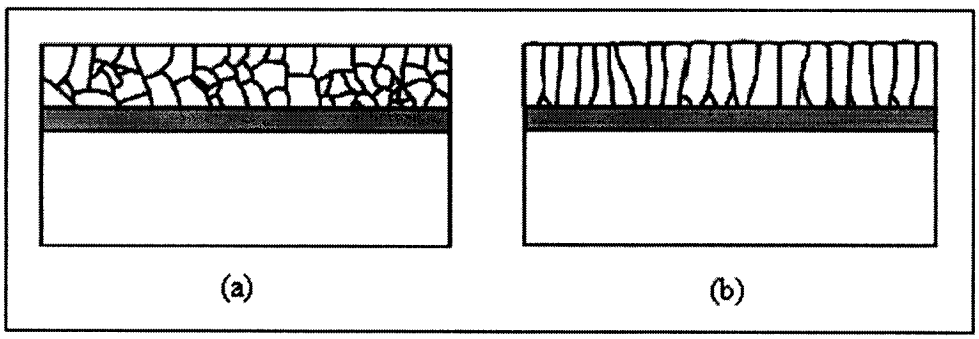

Fig.1.13. Two polycrystalline silicon structure (a) random grains (b) columnar [36]

As mentioned earlier, polysilicon has a considerably higher sensitivity than metal-based films, although not as high as the single-crystal silicon. Polysilicon has the advantage of being able to be deposited on various insulating layers. In applications where polysilicon is used as a piezoresistor, the grain structure is highly significant. The crystal orientation of individual grains as well as grain boundaries play crucial roles in this respect. Investigations have indicated that film textures are often dominated by a small number of orientations. Due to the highly anisotropic nature of piezoresistance in silicon, the dominant orientations can have a significant influence on the gauge factor of the material.

1.3.3 Post Processing

Post CMOS micro-machining consists of different steps taken on silicon wafer or die after the device has been fabricated. Multiple procedures can be performed as post-CMOS-processing such as photolithography, material etching, and material deposition. There are some key points to be considered when performing these process steps to insure proper operation of the final device. The steps taken must be compatible with CMOS technology i.e. they must be performed in low temperature and it should prevent contamination. Also in wet etching steps specific die areas must be protected against etching solution. For our device, the most important post micro- machining technique that has been predicted to release the device is chemical etching.

The etching process in CMOS and MEMS fabrication consists of removing a specific material by exposing the die to another substance, usually a liquid or gas that will selectively attack the target material. The main factor in this technique is the etch rate, which is defined as the thickness etched over time of etching. Although a high etch rate is usually desired in the manufacturing environment, for post-processing steps, if the etch rate is too high, the process may be very difficult to control and reproduce. It is very common to have etch rates on the order of hundreds or thousands of angstroms per minute.

Another important etching factor, especially in MEMS design is the selectivity of the etchant. Selectivity is the ratio of the etch rates for various materials. In many cases photoresist is used as the mask layer to protect specific areas of the die, so etchants must be selected that do not etch this photoresist mask.

The first factor to be taken into account when choosing an etchant is whether to use an isotropic or an anisotropic etchant. Some etchants are purely isotropic for some materials, which means they will etch the target material at the same rate in all directions. The other type of etchants, anisotropic, has different etch rates along different directions of the target material. Since almost all etchants, more or less attack the mask layers as well as the target material, for long etches, mask erosion and undercut may be a problem.

The next selection is whether to choose a wet or dry etching process. Wet etching is a purely chemical process that, if not performed carefully, can have serious drawbacks: poor process control, and excessive contamination to the system. However, wet etching can be highly selective. Moreover, unlike dry etching it does not need very special equipment. Wet etching is used to pattern a wide variety of materials. A table of common wet etchants and the corresponding target materials has been presented in Table1.1.

MATERIAL	WET ETCHANT	MASK
Si (Isotropic)	$HF + HNO_3 + Acetic(1:3:8)$	SiO_2 or Si_3N_4
Si (Anisotropic)	KOH , TMAH , EDP	SiO_2 or Si_3N_4
SiO_2	BHF	Photoresist
Si_3N_4	Hot Phosphoric Acid	SiO_2
Al	Phosphoric +Acetic + Nitric Acid	Photoresist
Cr	HCL	Photoresist
Au	KI	Photoresist

Table.1.1. Different etchants, their target materials and the corresponding masks [37]

The predicted post-processing techniques for releasing our device is a multi-masked wet etching process (more on this later)

CHAPTER 2 THEORY AND DESIGN CONSIDERATIONS

2.1 Partial Differential Equations Describing Deformation-Force Relationship

In the following sections we present the analytical description of the physical phenomena that have been used during the design and simulation of our design.

Assuming that the Cartesian coordinates of each point belong to a solid object is described by (x, y, z), if we apply a force (F_x, F_y, F_z), a deformation will appear in the object. As a result of this deformation the new coordinates of the point, will become $(x+u, y+v, z+w)$.

The resulting strain can be completely described by the deformation components (u, v, w) and their derivatives.

Following the small displacement assumption, the *normal and shear strain* components are given from the deformation as follows [38]:

$$\varepsilon_x = \frac{\partial u}{\partial x} \qquad \varepsilon_{xy} = \frac{\gamma_{xy}}{2} = \frac{1}{2}\left(\frac{\partial u}{\partial y} + \frac{\partial v}{\partial x}\right)$$

$$\varepsilon_y = \frac{\partial v}{\partial y} \qquad \varepsilon_{yz} = \frac{\gamma_{yz}}{2} = \frac{1}{2}\left(\frac{\partial v}{\partial z} + \frac{\partial w}{\partial y}\right) \qquad \text{(Eq.2.1)}$$

$$\varepsilon_z = \frac{\partial w}{\partial z} \qquad \varepsilon_{xz} = \frac{\gamma_{xz}}{2} = \frac{1}{2}\left(\frac{\partial u}{\partial z} + \frac{\partial w}{\partial x}\right)$$

The symmetric strain tensor ε, consists of both normal and shear strain components:

$$\varepsilon = \begin{bmatrix} \varepsilon_x & \varepsilon_{xy} & \varepsilon_{xz} \\ \varepsilon_{xy} & \varepsilon_y & \varepsilon_{yz} \\ \varepsilon_{xz} & \varepsilon_{yz} & \varepsilon_z \end{bmatrix} \qquad \text{(Eq.2.2)}$$

The resulting *stress* in the material is described by the symmetric stress tensor (Fig.2.1):

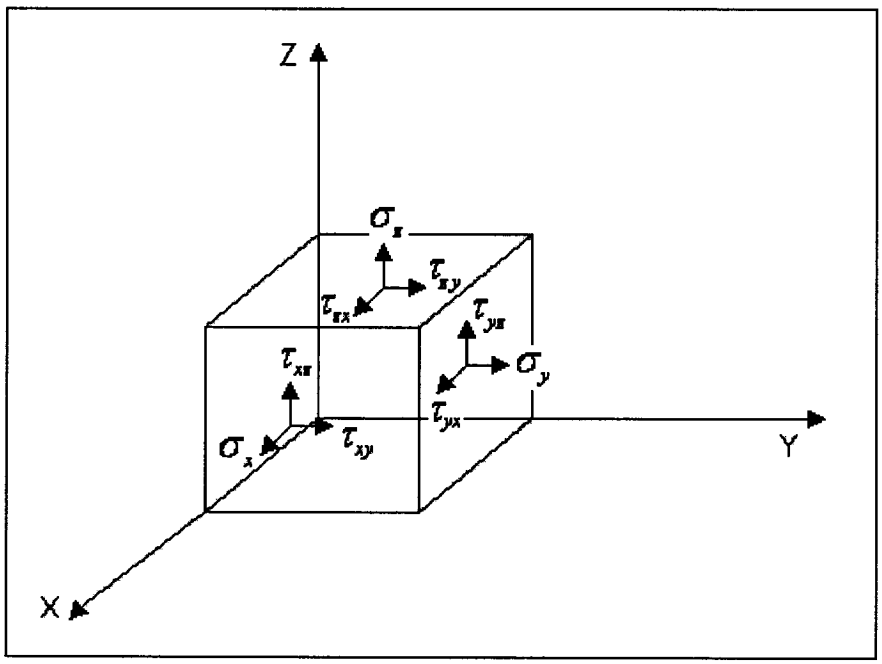

Fig.2.1. Normal and shear stresses applied to a differential element of a solid

$$\sigma = \begin{bmatrix} \sigma_x & \tau_{xy} & \tau_{xz} \\ \tau_{yx} & \sigma_y & \tau_{yz} \\ \tau_{zx} & \tau_{zy} & \sigma_z \end{bmatrix} \qquad \tau_{xy} = \tau_{yx} \qquad \tau_{xz} = \tau_{zx} \qquad \tau_{yz} = \tau_{zy} \qquad \text{(Eq.2.3)}$$

where σ 's are *normal stresses* and τ 's are *shear stresses*.

The relationship between stress and strain in a material in linear conditions and in tensor form is:

$$\sigma = D\varepsilon \qquad \text{(Eq.2.4)}$$

where D is called the *elasticity matrix*. D^{-1} can be described as:

$$D^{-1} = \frac{1}{E}\begin{bmatrix} 1 & -\nu & -\nu & 0 & 0 & 0 \\ -\nu & 1 & -\nu & 0 & 0 & 0 \\ -\nu & -\nu & 1 & 0 & 0 & 0 \\ 0 & 0 & 0 & 2(1+\nu) & 0 & 0 \\ 0 & 0 & 0 & 0 & 2(1+\nu) & 0 \\ 0 & 0 & 0 & 0 & 0 & 2(1+\nu) \end{bmatrix} \qquad \text{(Eq.2.5)}$$

In this equation E is the *Young's modulus* and ν is *Poisson's ratio* of the material. Therefore the extension of the stress-strain relationship will be as follows.

$$\begin{bmatrix} \sigma_x \\ \sigma_y \\ \sigma_z \\ \tau_{xy} \\ \tau_{yz} \\ \tau_{xz} \end{bmatrix} = \frac{E}{(1+\nu)(1-2\nu)}\begin{bmatrix} 1-\nu & \nu & \nu & 0 & 0 & 0 \\ \nu & 1-\nu & \nu & 0 & 0 & 0 \\ \nu & \nu & 1-\nu & 0 & 0 & 0 \\ 0 & 0 & 0 & \frac{1-2\nu}{2} & 0 & 0 \\ 0 & 0 & 0 & 0 & \frac{1-2\nu}{2} & 0 \\ 0 & 0 & 0 & 0 & 0 & \frac{1-2\nu}{2} \end{bmatrix} \bullet \begin{bmatrix} \varepsilon_x \\ \varepsilon_y \\ \varepsilon_z \\ \gamma_{xy} \\ \gamma_{yz} \\ \gamma_{xz} \end{bmatrix} \qquad \text{(Eq.2.6)}$$

In a real problem the known input to the system is the volume forces (body forces) and therefore our goal is to find the relationship between the deformation components (u, v, w) and the volume force components (F_x, F_y, F_z), which in turn enables us to find the resulting strain and stress components.

The required equation is known as *Equilibrium equations*:

$$\begin{aligned} -\frac{\partial \sigma_x}{\partial x} - \frac{\partial \tau_{xy}}{\partial y} - \frac{\partial \tau_{xz}}{\partial z} &= F_x \\ -\frac{\partial \tau_{xy}}{\partial x} - \frac{\partial \sigma_y}{\partial y} - \frac{\partial \tau_{yz}}{\partial z} &= F_y \\ -\frac{\partial \tau_{xz}}{\partial x} - \frac{\partial \tau_{yz}}{\partial y} - \frac{\partial \sigma_z}{\partial z} &= F_z \end{aligned} \qquad \text{(Eq.2.7)}$$

Using compact notation, this can be written as:

$$-\nabla \cdot \sigma = F \qquad \text{(Eq.2.8)}$$

If we substitute, stress-strain and strain-deformation relationship from previous equations we will reach the *Navier's equation of equilibrium* expressed in the displacements:

$$-\nabla \cdot (c\nabla u) = F \qquad \text{(Eq.2.9)}$$

2.2 Piezoresistivity

Piezoresistivity is a material property where the bulk resistivity of the material changes as a function of the applied mechanical stresses.

The physical explanation of the phenomenon in terms of the change in energy band gap between the valance and the conduction bands and the shape of E-k curves, in the material under stress is as follows.

2.2.1 Quantum Mechanics Explanation of Piezoresistivity

A mechanical stress applied to a crystalline solid is accompanied by a strain. This strain deforms the crystalline structure and breaks symmetry [39,40]. The destruction of the symmetry has some noticeable effects on the electronic band structure of the material.

Electron wave functions in the crystal have the same periodicity as the lattice, and therefore the same symmetry. Fig.2.2 shows the valence and conduction band configuration of Silicon for different crystalline directions.

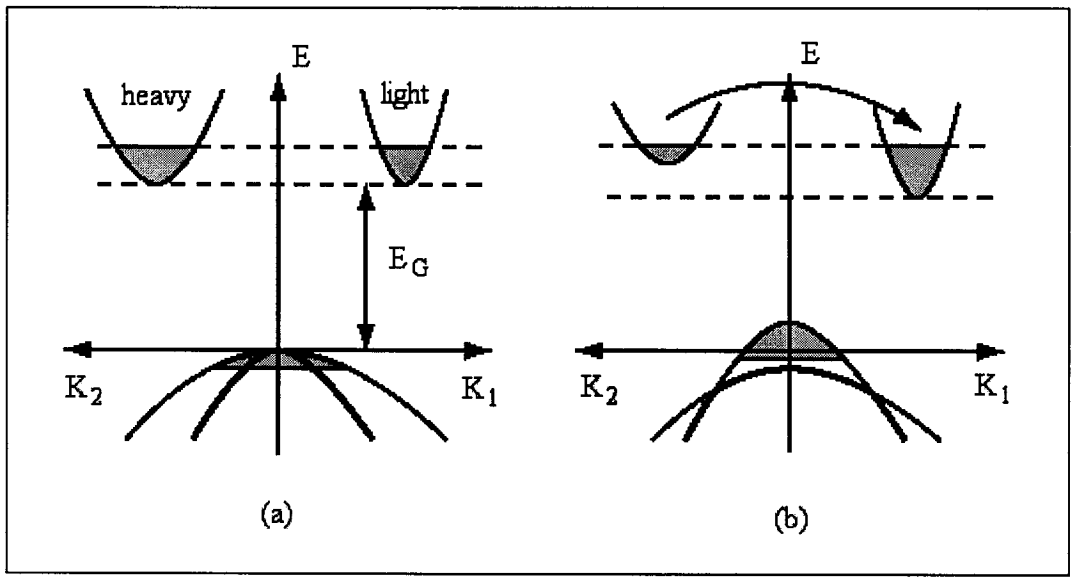

Fig.2.2. Energy band gap configurations in a crystalline material in different directions (a) without strain (b) with strain

The upper half of Fig.2.2 (a) shows two edges of the conduction band, filled with electrons, and in the lower half two edges of the valence bands, filled with holes. Depending on the current direction, electrons and holes in one band for one direction are heavier than those in equivalent band of the other direction. The edges are separated by the band-gap energy E_G. When stress is present, due to the change of lattice constant in different directions, the equivalent edges are no longer on the same level and shift up-and-downwards (Fig.2.2 (b)). This modifies the original band-gap. And consequently changes the value of n_i that is an important factor in determining the carrier concentrations inside the material. The changing gap and density of states modify the number of thermally excited charge carriers [43]

$$n_i^2 = N_c N_V \exp\left[\frac{-E_G}{kT}\right] \qquad \text{(Eq.2.10)}$$

In addition, this starts a redistribution of charge from far bands to bands closer to the gap, which changes their effective mass. Finally, the valence bands also change in shape, meaning another effective mass change and a modification in the density of states.

$$\frac{1}{m^*} = \frac{1}{\hbar^2}\frac{d^2E}{dk^2} \qquad \text{(Eq.2.11)}$$

The changing masses modify the mobilities of electrons and holes. The effective masses and band-gaps are determinative factors in the material's electronic transport properties. Both concentrations and mobilities appear in the conductivity:

$$\sigma = e(n\mu_n + p\mu_p) \qquad \text{(Eq.2.12)}$$

where, e is the unit charge, n and p are the total electron and hole concentrations, respectively, and μ_n and μ_p are electron and hole mobilities. The mobilities are a weighted average over all bands. It should also be noted that under stress, the conductivity of silicon is no longer isotropic, which makes the tensor notation necessary.

2.2.2 Tensor Equations Describing Piezoresistance Effect

In a 3D anisotropic crystal, the electric field vector E is related to the current density vector J by a 3x3 *resistivity tensor* [39].

$$E = \rho \cdot J \qquad \text{(Eq.2.13)}$$

$$\begin{bmatrix} E_x \\ E_y \\ E_z \end{bmatrix} = \begin{bmatrix} \rho_1 & \rho_6 & \rho_5 \\ \rho_6 & \rho_2 & \rho_4 \\ \rho_5 & \rho_4 & \rho_3 \end{bmatrix} \bullet \begin{bmatrix} J_x \\ J_y \\ J_z \end{bmatrix} \qquad \text{(Eq.2.14)}$$

In a piezoresistive material, these six resistivity components depend on the stress in the material, and restricting our discussion to the case of isotropic materials, we can represent the changes in the component values due to stress as:

$$\begin{bmatrix} \rho_1 \\ \rho_2 \\ \rho_3 \\ \rho_4 \\ \rho_5 \\ \rho_6 \end{bmatrix} = \begin{bmatrix} \rho \\ \rho \\ \rho \\ 0 \\ 0 \\ 0 \end{bmatrix} + \begin{bmatrix} \Delta\rho_1 \\ \Delta\rho_2 \\ \Delta\rho_3 \\ \Delta\rho_4 \\ \Delta\rho_5 \\ \Delta\rho_6 \end{bmatrix} \qquad \text{(Eq.2.15)}$$

The piezoresistance effect can now be described by relating each of the six fractional resistivity changes $\Delta\rho_i / \rho$ to each of the six stress components. Mathematically this yields to a 6x6 matrix of 36 coefficients. By definition, the elements of this matrix are called *piezoresistance coefficients*, π_{ij} expressed in Pa^{-1}.

For crystalline materials, the symmetry conditions lead to certain relations between the different matrix components, which reduce the number of independent, non-vanishing components to considerably less than 36. For the cubic crystal structure of Silicon and Germanium, three different coefficients remain, $\pi_{11}, \pi_{12}, \pi_{44}$, and the matrix takes the following form:

$$\frac{1}{\rho}\begin{bmatrix} \Delta\rho_1 \\ \Delta\rho_2 \\ \Delta\rho_3 \\ \Delta\rho_4 \\ \Delta\rho_5 \\ \Delta\rho_6 \end{bmatrix} = \begin{bmatrix} \pi_{11} & \pi_{12} & \pi_{12} & 0 & 0 & 0 \\ \pi_{12} & \pi_{11} & \pi_{12} & 0 & 0 & 0 \\ \pi_{12} & \pi_{12} & \pi_{11} & 0 & 0 & 0 \\ 0 & 0 & 0 & \pi_{44} & 0 & 0 \\ 0 & 0 & 0 & 0 & \pi_{44} & 0 \\ 0 & 0 & 0 & 0 & 0 & \pi_{44} \end{bmatrix} \bullet \begin{bmatrix} \sigma_x \\ \sigma_y \\ \sigma_z \\ \tau_{yz} \\ \tau_{xz} \\ \tau_{xy} \end{bmatrix} \qquad \text{(Eq.2.16)}$$

Combining Eq.2.16 and Eq.2.14 and Eq.2.16 leads to the following relations:

$$\rho_1 = \rho[1+\pi_{11}\sigma_x + \pi_{12}(\sigma_y + \sigma_z)]$$

$$\rho_2 = \rho[1+\pi_{11}\sigma_y + \pi_{12}(\sigma_x + \sigma_z)]$$

$$\rho_3 = \rho[1+\pi_{11}\sigma_z + \pi_{12}(\sigma_x + \sigma_y)] \qquad \text{(Eq.2.17)}$$

$$\rho_4 = \rho\pi_{44}\tau_{yz}$$

$$\rho_5 = \rho\pi_{44}\tau_{xz}$$

$$\rho_6 = \rho\pi_{44}\tau_{xy}$$

Although Mathematically, the relationship between stress in the material and the resulting change in the resistivity, has been derived, we prefer, for simulation purposes, to have the relationship in the form of:

$$J = \rho^{-1} \cdot E \qquad \text{(Eq.2.18)}$$

in which ρ^{-1} is the *conductivity matrix*. Doing the necessary calculations, we will have:

$$\rho^{-1} = \frac{1}{\det \rho}\begin{bmatrix} \rho_2\rho_3 - \rho_4^2 & \rho_4\rho_5 - \rho_3\rho_6 & \rho_4\rho_6 - \rho_2\rho_5 \\ \rho_4\rho_5 - \rho_3\rho_6 & \rho_1\rho_3 - \rho_5^2 & \rho_5\rho_6 - \rho_1\rho_4 \\ \rho_4\rho_6 - \rho_2\rho_5 & \rho_5\rho_6 - \rho_1\rho_4 & \rho_1\rho_2 - \rho_6^2 \end{bmatrix} \qquad \text{(Eq.2.19)}$$

where:

$$\det \rho = \rho_1\rho_2\rho_3 + 2\rho_4\rho_5\rho_6 - \rho_2\rho_5^2 - \rho_1\rho_4^2 - \rho_3\rho_6^2 \qquad \text{(Eq.2.20)}$$

2.2.3 Temperature and Doping Level Dependency of Piezoresistance Effect

Piezoresistance coefficients of silicon are functions of both impurity concentration and temperature. Fig.2.3 shows the decrease of π_{11} with the increase of the impurity concentration N for an n-type silicon sample.

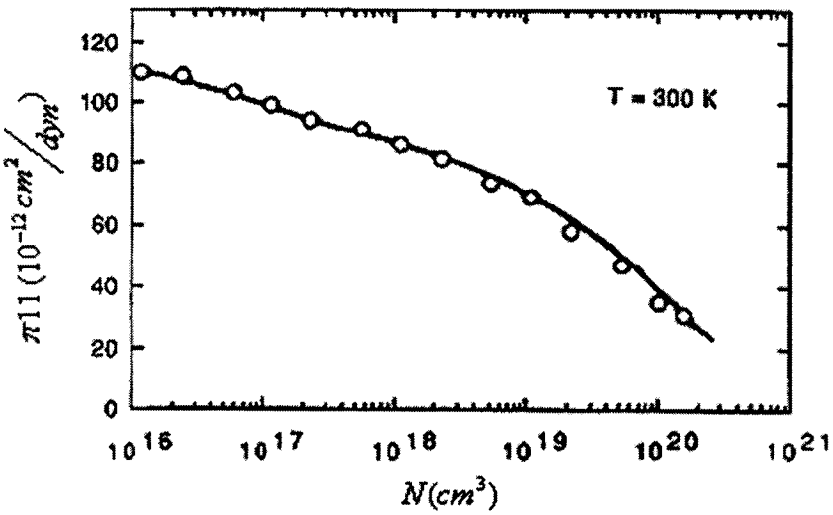

Fig.2.3. π_{11} versus impurity concentration in n-type Silicon [39]

From Fig.2.3 it can be concluded that to keep a reasonably high gauge factor, the lower amounts of doping level should be chosen.

On the other hand, any piezoresistive coefficient can be expressed as its low-doped room temperature value, known as π_0 multiplied by a factor *P(N,T)* that is a function of impurity concentration and temperature.

$$\pi(N,T) = \pi_0 \cdot P(N,T) \qquad \text{(Eq.2.21)}$$

Fig.2.4 shows the Piezoresistance factor *P(N,T)* for a p-type Silicon. This figure summarizes the discussion as: The piezoresistance effect decreases with increasing

doping concentration and with increasing temperature. But the decreasing distance between the curves indicates that the temperature coefficient of the piezoresistivity also decreases with increasing doping concentration. In practice, sensitivity is often sacrificed to obtain a lower temperature coefficient, and therefore to increase the stability of the sensor.

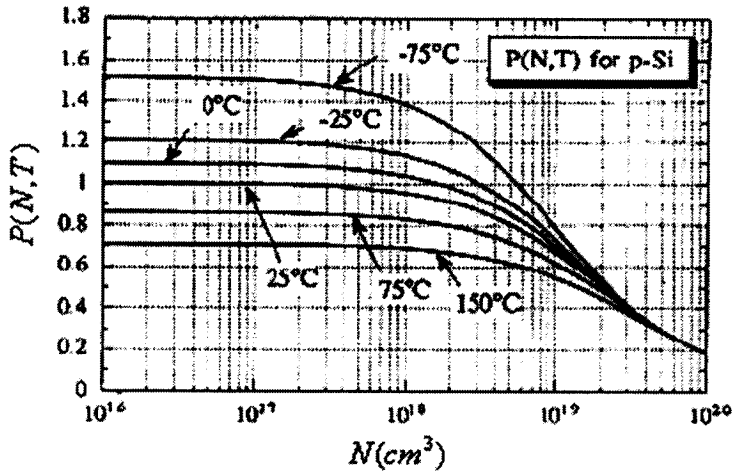

Fig.2.4. Piezoresistance factor *P(N,T)* as a function of impurity concentration and temperature for p-type Silicon [39]

2.3 Mathematical Analysis of Strain in a Cantilever

Although we use the mentioned tensor equations relating force-displacement-strain-stress and piezoresistivity for simulating the mechanical and electrical behavior of our device; from a design point of view, they do not offer enough guidelines to be used in selecting the geometries. Therefore in this stage, we narrow our discussion and utilize *simple theory of bending* [41] to analyze the mechanical behavior of a beam subject to a concentrated load. In the following discussion the words "beam" and "cantilever" are used interchangeably.

2.3.1 The Assumptions of the Simple Theory of Bending

(1) The beam is initially straight and unstressed.

(2) The material of the beam is perfectly homogenous and isotropic, i.e. of the same density and elastic properties throughout.

(3) The elastic limit is nowhere exceeded.

(4) Young's modulus for the material is the same in tension and compression.

(5) Plane cross sections remain plain before and after bending.

(6) Every cross section of the beam is symmetrical about the plane of bending, i.e. about an axis perpendicular to the N.A.

(7) There is no resultant force perpendicular to any cross-section.

2.3.2 Simple Theory of Bending

Let's consider a beam initially unstressed and subject to a constant bending moment (B.M) along its length, or pure bending. Fig.2.5 (a) shows the cross section of the beam in the plane of bending. After applying the force the beam will bend to a radius R as shown in Fig.2.5 (b). Considering a fiber like AB, distance y from the neutral axis (N.A), according to the simple theory of bending the relationship between M (bending moment), I (second moment of area of the beam cross section), σ (stress in fiber AB), E (Modulus of elasticity or Young's Modulus), R (radius of curvature) and y (distance between fiber AB and Neutral axis) will be:

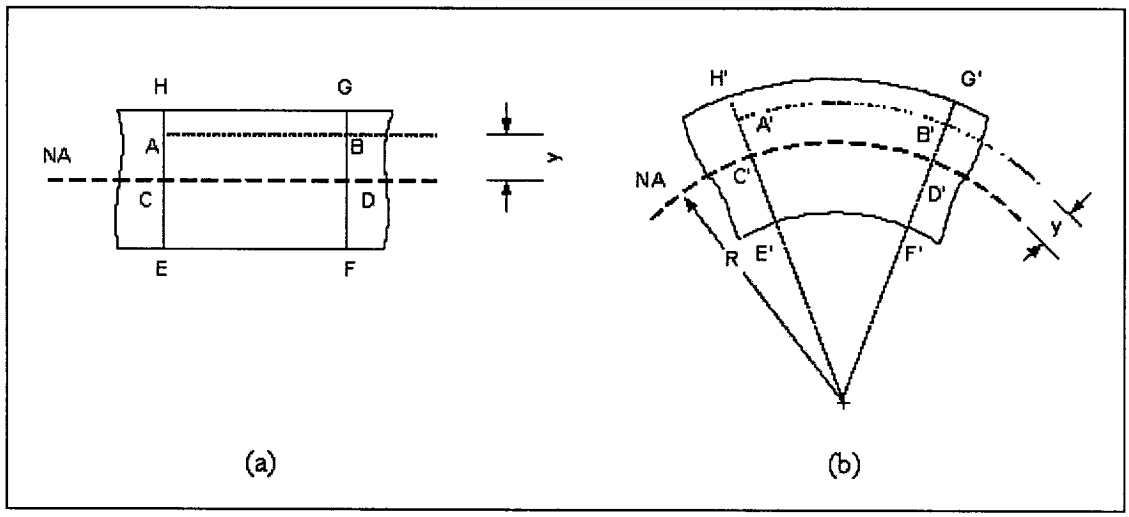

Fig.2.5. Cross section of a beam in the plane of bending (a) before bending (b) after bending

$$\frac{M}{I} = \frac{\sigma}{y} = \frac{E}{R} \qquad \text{(Eq.2.22)}$$

In which:

$I = \int y^2 dA$ (dA is the area of the strip in Fig.2.6) (Eq.2.23)

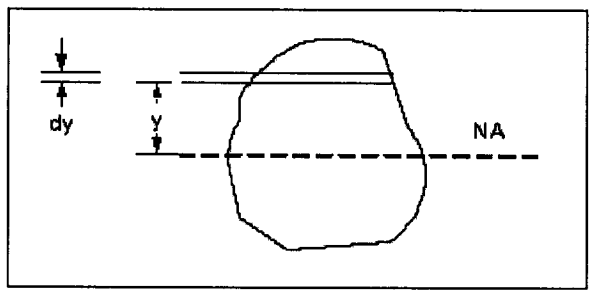

Fig.2.6. Cross section of the beam (perpendicular to the plane of bending)

2.3.3 Relationship Between Loading, Shearing Force, Bending Moment, Slope and Deflection

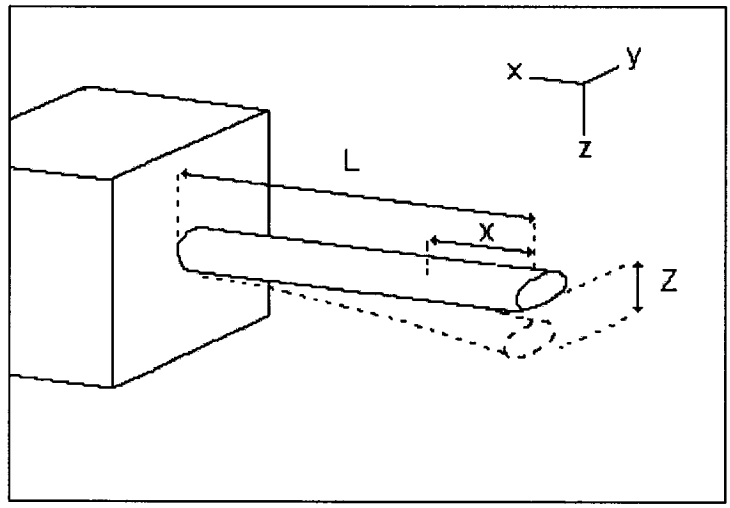

Fig.2.7. Bending of a simple cantilever with arbitrary (but uniform and symmetric) cross section

If a beam that is initially horizontal when unloaded, deflects to a new position under load, and assuming that the deflection is small and EI is constant along the beam (Fig.2.7), we have these relationships:

Deflection = z

Slope = $\frac{dz}{dx}$

Bending moment = $EI\frac{d^2z}{dx^2}$ (Eq.2.24)

Shear force = $EI\frac{d^3z}{dx^3}$

Load distribution = $EI\frac{d^4z}{dx^4}$

2.3.4 Bending in a Simple Cantilever

Now if we consider a simple cantilever with length L, a rectangular cross section with a constant EI and a concentrated load F at the end (Fig.2.8), we will have:

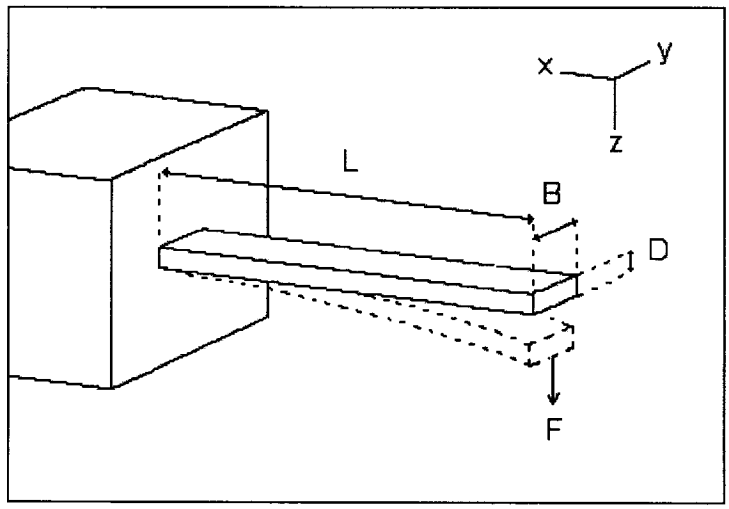

Fig.2.8. Bending of a simple cantilever with uniform rectangular cross section

$$I = \frac{BD^3}{12} \qquad \text{(Eq.2.25)}$$

$$M_{xx} = EI\frac{d^2z}{dx^2} = Fx \quad \Rightarrow \quad EI\frac{dz}{dx} = \frac{Fx^2}{2} + k_1 \quad \Rightarrow$$

$$EIz = \frac{Fx^3}{6} + k_1x + k_2$$

At $x = L$, $\frac{dz}{dx} = 0 \Rightarrow k_1 = \frac{-FL^2}{2}$ and At $x = L$, $z = 0$

$$\Rightarrow k_2 = \frac{FL^3}{3}$$

Deflection: $$z = \frac{F}{EI}\left[\frac{1}{6}x^3 - \frac{L^2}{2}x + \frac{L^3}{3}\right] \qquad \text{(Eq.2.26)}$$

Slope: $$\frac{dz}{dx} = \frac{F}{EI}\left[\frac{1}{2}x^2 - \frac{L^2}{2}\right] \quad \text{(Eq.2.27)}$$

Bending moment: $$\frac{d^2z}{dx^2} = \frac{F}{EI}x \quad \text{(Eq.2.28)}$$

$$\Rightarrow \frac{d^2z}{dx^2}(\max) = \frac{FL}{EI} \quad \text{at} \quad x = L \quad \text{(Eq.2.29)}$$

On the other hand the second derivative of the displacement at each point of the beam is related to the radius of the curvature of the beam at that point by this equation:

$$\frac{d^2z}{dx^2} \propto \frac{1}{R} \quad \Rightarrow \quad \frac{d^2z}{dx^2} = \frac{\alpha}{R} \quad \text{(Eq.2.30)}$$

where α is the constant of proportionality.

Therefore the following conclusions can be drawn:

1) The relationship between all $z, \frac{dz}{dx}, \frac{d^2z}{dx^2}$ and F is linear.

2) Considering Eq.2.30 we have the maximum curvature and therefore the maximum stress and strain at the fixed end (next to the base) of the cantilever. Therefore to achieve the maximum sensitivity, we should consider the lower or upper surface of the beam at the maximum strain area, as the position of our strain sensor (i.e. piezoresistor) (Fig.2.9)

3) Assuming a constant F:

Increasing of L results to increasing of the maximum strain.

Decreasing of E (by selecting a softer material) increases the maximum strain.

Decreasing of B decreases I and so increases maximum strain.

According to Eq.2.25 and the fact that strain in a fiber, distance y from the N.A is:

Form Eq.2.22 $\Rightarrow \varepsilon = \frac{\sigma}{E} = \frac{y}{R}$ (Eq.2.31)

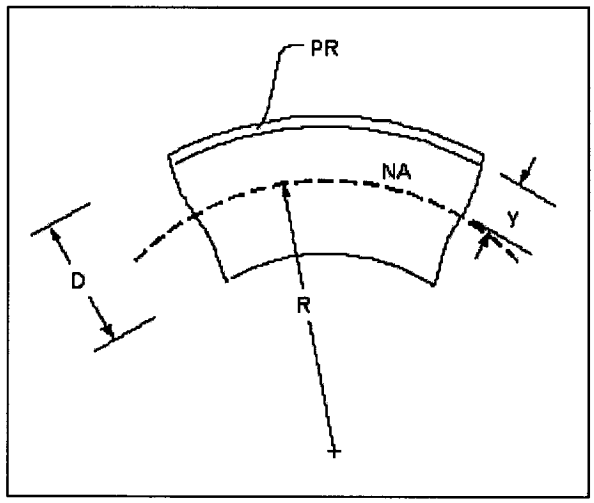

Fig.2.9. The optimum position of the stress sensor with respect to the beam

Assuming that we can place a very thin piezoresistor at the upper surface of the beam (Fig.2.9) at the most stressed zone (next to the fixed end of the beam) the strain for the fibers of the sensor will be:

$$\varepsilon(x=L) = \frac{y}{R} \approx \frac{D/2}{\alpha \frac{EI}{FL}} = \frac{DFL}{2\alpha E\left(\frac{BD^3}{12}\right)} = \frac{6FL}{\alpha EBD^2} \quad \text{(Eq.2.32)}$$

Therefore to achieve more strain we should reduce D as much as possible. The effect of reducing D on strain is the most important factor (to the power 2). It should be mentioned that in practice, the thickness of the sensor should be taken into account and in this case the increase in the strain due to decrease in thickness will be smaller (due to the shift of NA toward the sensor).

2.3.5 Bending in a More Complicated Cantilever

Now let's consider a more practical cantilever with a tapered free end and a rectangular hole of length $(L - L_3)$ and Width B' which is produced to increase strain at the fixed end of the beam (Fig.2.10)(based on Eq.2.29). To deduce deflection, slope and bending moment equations for this beam we should divide the length of the beam to several intervals and write the equations for each interval separately. Assume that Load F is a concentrated load and is applied to a point distance L_1 from the free end of the beam.

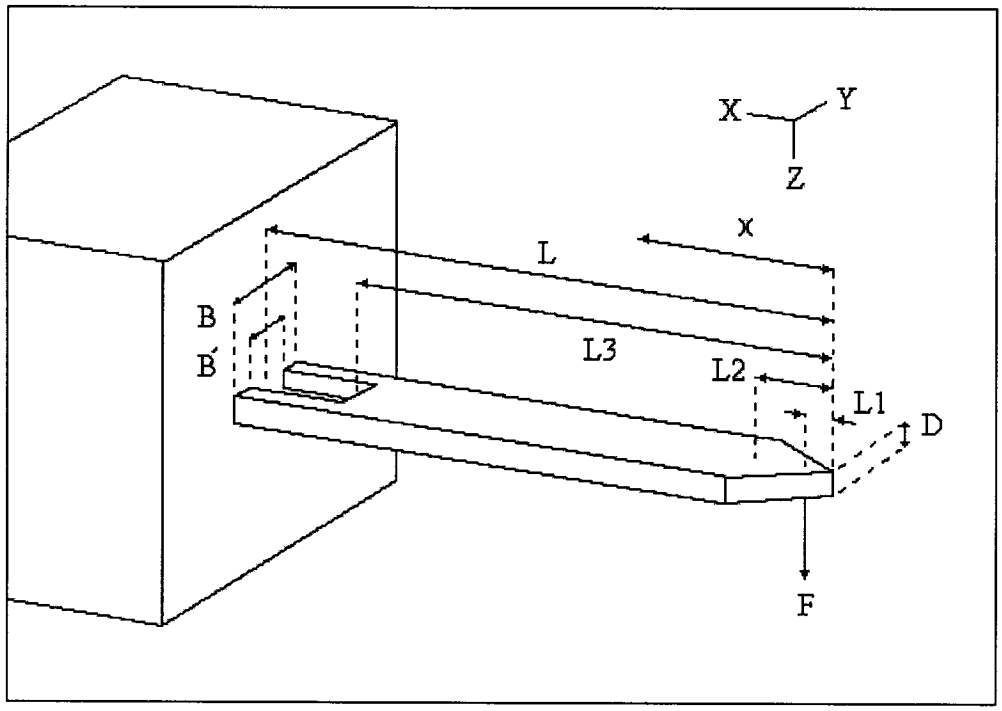

Fig.2.10. A cantilever beam suitable for AFM applications

- for $0 \le x < L_1$: $EI\dfrac{d^2 z_1}{dx^2} = 0 \quad \Rightarrow \quad \dfrac{dz_1}{dx} = c_1 \quad \Rightarrow \quad z_1 = c_1 x + c_2$

- for $L_1 \le x < L_2$: $EI_{(x)}\dfrac{d^2 z_2}{dx^2} = F(x - L_1)$ in which : $I_{(x)} = \dfrac{BD^3}{12L_2}x$

$$\Rightarrow \quad \text{if} \quad \frac{12L_2F}{EBD^3} = m \quad \Rightarrow \quad \frac{d^2z_2}{dx^2} = m(1-\frac{L_1}{x})$$

$$\Rightarrow \frac{dz_2}{dx} = m(x - L_1 \ln x + c_3) \quad \Rightarrow z_2 = m\left(\frac{1}{2}x^2 + c_3x + c_4 - L_1 x \ln x\right)$$

♦ for $L_2 \le x < L_3$: $EI\frac{d^2z_3}{dx^2} = F(x-L_1)$ in which $I = \frac{BD^3}{12}$

$$\Rightarrow \frac{dz_3}{dx} = \frac{F}{EI}\left(\frac{1}{2}x^2 - L_1x + c_5\right) \quad \Rightarrow z_3 = \frac{F}{EI}\left(\frac{1}{6}x^3 - \frac{L_1}{2}x^2 + c_5x + c_6\right)$$

♦ for $L_3 \le x \le L$: $EI\frac{d^2z}{dx^2} = F(x-L_1)$ in which $I = \frac{(B-B')D^3}{12}$

$$\Rightarrow \frac{dz}{dx} = \frac{F}{EI}\left(\frac{1}{2}x^2 - L_1x + c_7\right) \quad \Rightarrow z = \frac{F}{EI}\left(\frac{1}{6}x^3 - \frac{L_1}{2}x^2 + c_7x + c_8\right)$$

By considering the following boundary conditions we can determine $c_1, c_2, ..., c_8$.

At $x = L$: $z = 0$ & $\frac{dz}{dx} = 0$ $\Rightarrow c_7, c_8$

At $x = L_3$: $z_3 = z$ & $\frac{dz_3}{dx} = \frac{dz}{dx}$ $\Rightarrow c_5, c_6$

At $x = L_2$: $z_2 = z_3$ & $\frac{dz_2}{dx} = \frac{dz_3}{dx}$ $\Rightarrow c_3, c_4$

At $x = L_1$: $z_1 = z_2$ & $\frac{dz_1}{dx} = \frac{dz_2}{dx}$ $\Rightarrow c_1, c_2$

By a similar discussion we can conclude that (assuming the simple theory of bending):

1) The maximum curvature and therefore the maximum strain will happen at the fixed end of the cantilever.

2) Compared to the similar cantilever but without a rectangular hole, the average strain in the interval $L_3 \leq x \leq L$ has been increased by a factor $\frac{B}{B-B'}$.

3) Deflection and therefore strain at the end of the beam, is not affected by the shape of the beam around the tip.

There are other factors that affect selecting of dimensions and designing of the cantilever. Some of them are:

- Limited accuracy of simple theory of bending due to it's simplifying assumptions.
- Non-uniform stress concentration in some areas, that does happen in practice, but cannot be explained by the simple method described above.
- Dependency of dimensions to applications.
- The eigenfrequencies of the beam that limits the operational speed of the final system

The first two factors will be compensated using *Finite Element Method (FEM)* analysis of the design. The third factor is considered in the design. And the following discussion studies the eigenfrequencies of the beam.

2.3.6 Cantilever Eigenfrequencies

Bending Eigenfrequencies of a simple cantilever (Fig.2.8) is determined by [42]:

$$\omega_j = \frac{j^2\pi^2}{L^2}\sqrt{\frac{EI_z}{\rho A}} \qquad j = 1,2,3,.... \qquad \text{(Eq.2.33)}$$

$$I_z = \frac{BD^3}{12} = \frac{AD^2}{12} \quad \Rightarrow \quad \omega_j = \frac{j^2\pi^2 D}{L^2}\sqrt{\frac{E}{12\rho}} \qquad \text{(Eq.2.34)}$$

The vibrations of a simple beam in its first four bending eigenfrequencies are shown in Fig.2.11.

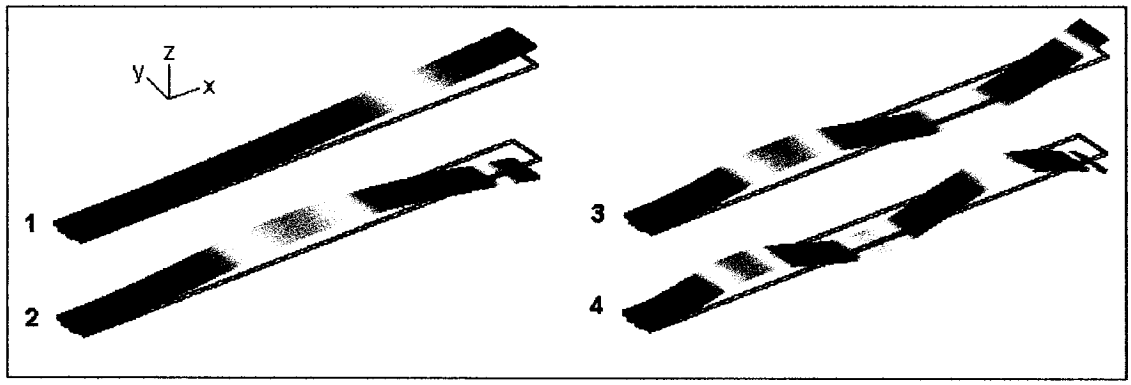

Fig.2.11. The vibrations of a beam in the first four eigenfrequencies

Therefore it is obvious that for the simple beam, increasing L and decreasing D and E, which mentioned as the provisions for increasing the maximum strain, all have negative effects on the natural frequency of the beam. Based on their position in Eq.2.33, we can order the negative effect of these factors as:

1- Increasing L, which decreases the natural frequency of the beam by power 2.

2- Decreasing D, that decreases the natural frequency by the same rate.

3- Decreasing E, which decreases the natural frequency by power ½.

The only factor that increases the maximum strain and has no effect on the natural frequency is decreasing of B.

2.4 The Facts and Limitations to Be Taken into Account

1. The maximum curvature and therefore the maximum stress and strain happen at the fixed end of the cantilever (Eq.2.29).
2. Considering the overall structure of the design, the more distance of the sensor part from the neutral plane results in more sensitivity.
3. The increase of sensitivity can be accomplished by increasing L, and decreasing E, B, and D (the most important factor) (Eq.2.32).
4. The increase of sensitivity by changing the geometry parameters (item c) negatively affects the eigenfrequencies of the beam (Eq.2.33). Therefore a compromise should be achieved.
5. The only factor that increases the maximum strain and does not alter the eigenfrequencies, is the decreasing of B (Eq.2.32, 33)
6. In any standard technology that is practically used to fabricate the sensor, the number, the order, the material, and the thickness of layers are fixed and cannot be changed by a designer.
7. The selection of the layers should satisfy the condition of having both mechanical connection and electrical isolation between the frame of the cantilever and the sensor part, to make the probe functional.
8. Residual stress between the layers should be avoided or at least minimized.

CHAPTER 3 PROBE STRUCTURE AND MODELING RESUTS

3.1 Description of the Recommended Design for the Probe

The first step in the design process is to select the layers, which should be used to construct different parts of the probe. A frame and a sensor are the minimum required parts, but as mentioned, an interface should exist as well, to establish both the mechanical connection and electrical isolation between the frame and the sensor. Among different layers in CMOSP35 technology, only the SiO_2 layers are insulators, and therefore they are the only candidates for the interface part. The frame can be constructed from SiO_2, Polysilicon or metal layers as well as their combinations. Although both metal layers and Poly layers can be used as the sensor part, regarding the theory section about comparison of piezoresistivity in polysilicon and metals, polysilicon layers are the best options for sensor part.

After studying different possible combinations of the layers and taking into account all of the mentioned design considerations, Ploy1 was selected as the frame, Poly 2 as the sensor and the intermediate Oxide between Poly1 and Poly as the interface layer.

The general outline of the proposed cantilever is a tapered 160 μm × 25 μm rectangle with a rectangular opening in the middle of the sensor parts (beginning at the fixed end of the beam). The widths of the Poly2 piezoresistors and the metal parts along the resistor as well as the lateral distance between adjacent resistor branches are 0.8 μm everywhere. Fig.3.1 displays a general schematic of the recommended probe with its dimensions.

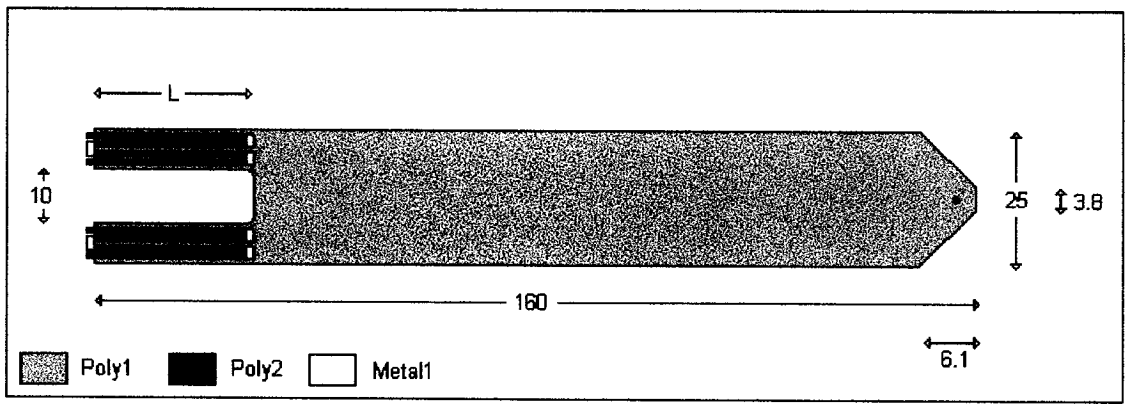

Fig.3.1. The general shape of the proposed design (The dimensions are in μm)

The existence of this opening confines the stress and intensifies it in its contiguous areas, on top of which we intend to place the sensors.

Table.3.1 contains the thickness information of the layers in CMOSP35 technology. The relative thickness of the chosen layers (0.275 μm for Poly1, 0.18 μm for Poly2 and 0.037 μm for the intermediate Oxide) results in positioning the sensor part completely above the neutral plane of the structure.

LAYER	*THICKNESS (Å)*
Thin/Thick Oxide	1800/2800
Poly1	2750
Oxide	370
Poly2	1800
Oxide	4280
Metal1	6650
Oxide	10000
Metal2	6400
Oxide	10000
Metal3	6400
Oxide	10000
Metal4	9250

Table.3.1. Thickness of the layers in CMOSP35 Technology

This combination also produces the thinnest possible cross section of the device, which is a very important factor in sensitivity.

Also eliminating all metal layers and almost all Oxides (except intermediate layer between Poly1 and Poly2) has produced a structure with the least possible residual stress and therefore prevents the unwanted deformation of the beam.

A common drawback of the traditional meander-like strain gauges is the negative effect of the turning (transverse) parts on sensitivity. While in the longitudinal branches of the sensor, the strain is in the same direction of the electrical current, in the transverse parts, strain and current are perpendicular. Taking into account the piezoresistive coefficients of the material, this phenomenon attenuates the overall performance of the gauge. In our design we have suppressed this drawback by taking advantage of the 3D structure of the target fabrication technology. The transverse parts have been replaced with bridge-like structures built of the combination of 'Metal1' and 'Contact'. This structure establishes the required electrical connection between the resistor branches without exhibiting any attenuating effect. The resulted form of the sensor has been shown in Fig.3.2.

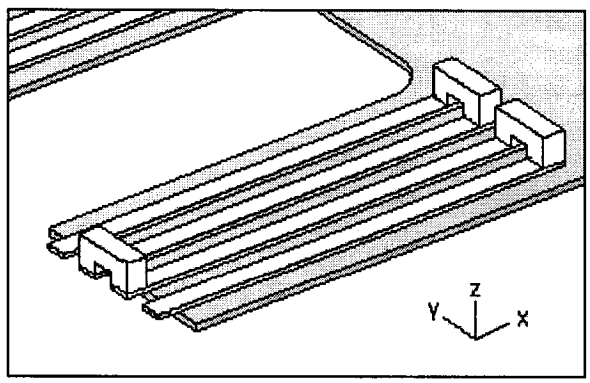

Fig.3.2. The combination of Poly2 layers and Metal bridges that forms the sensor part of the probe

Even though the doping level of the Poly layers in CMOS technology, is not disclosed by manufacturers, the estimation below shows that the Poly layers have been highly doped to reach high values of conductivity. As it is known, high level of doping increases temperature stability of the sensor response. However, if this level of temperature stability is not found sufficient for some specific applications, the proposed structure makes it also possible to further dope the sensor parts in the post-processing steps, and thus, make it more stable.

The emergence of the piezoresistive sensor parts also makes it possible to passivate the surface of the piezoresistive sensor parts using soft organic materials and therefore to prevent degradation of sensor characteristics in working environment, with time.

In the following discussion we study the mechanical and electrical characteristics of the proposed design. We utilized the finite element method analysis capabilities of FEMLAB software to model the characteristics of the proposed design. Wherever analytical calculations were possible, the simulation results have been compared to and approved by the analytical results. Also some simple test devices have been modeled for this purpose. For memory and solution time considerations, we have used the symmetry property of the probe to do the simulation on one half of the proposed design structure. By applying proper boundary values, the results are valid for the complete structure.

3.2 Neutral Plane and Stress Distribution

The first important factor, which is crucial for the proper operation of the AFM piezoresistive probe is that the sensor part should be located completely at one side of the neutral axis. Otherwise both tension and compression will be produced inside the sensor and the net stress in the sensor will be reduced.

Fig.3.3 shows the cross section of the probe at sensor areas. The dark red zones represent those areas having the maximum strain, where, are the location of the sensor. Because the strain and the resulted stress in the frame are dominantly composed of x-direction strain and stress (at least more than ten times greater than normal and shear components in other directions), the graphs are drawn for normal strain and stress in x-direction, however in the tensor calculations for computing the change of the resistance, sensitivity, etc. all of the components have been taken into account.

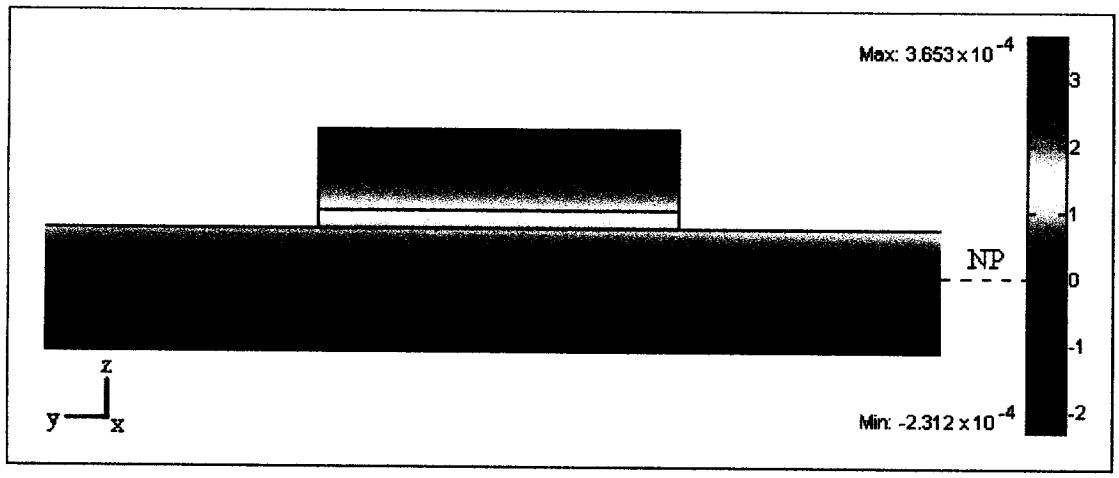

Fig.3.3. Normal strain in x-direction in one y-z cross section of the device in sensor areas

Fig.3.4 displays the corresponding normal stress in x-direction for the same cross section and Fig.3.5 is the numerical graph that shows the amount of stress for different points of line AB in Fig.3.4 versus the distance of the point from the top of Poly1. The linear change of stress in vertical direction in each layer is obvious in this graph. Also is should be noticed that while strain is a continuous quantity and changes smoothly in vertical direction inside the structure, the corresponding stress is not. The reduction of stress in Oxide layer can be seen in Fig.3.5.

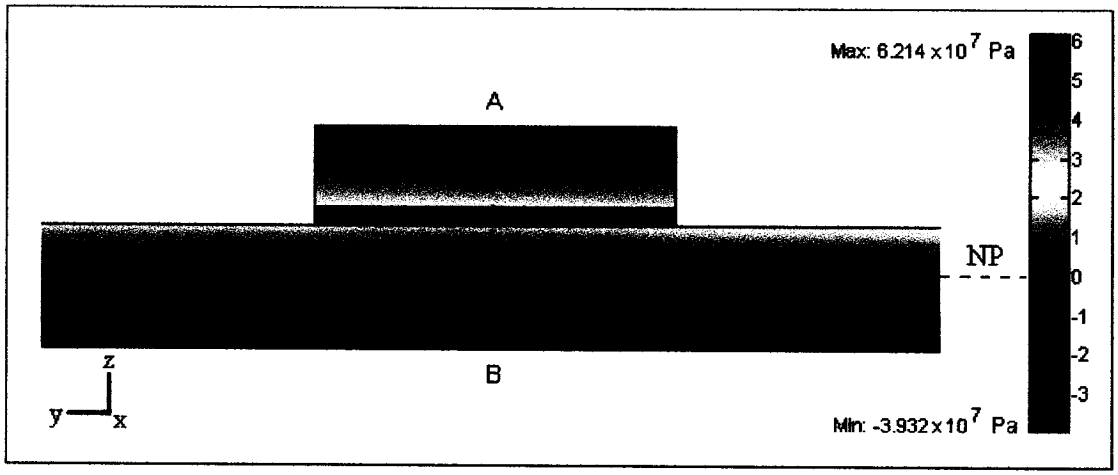

Fig.3.4. Normal stress in x-direction in one y-z cross section of the device in sensor areas

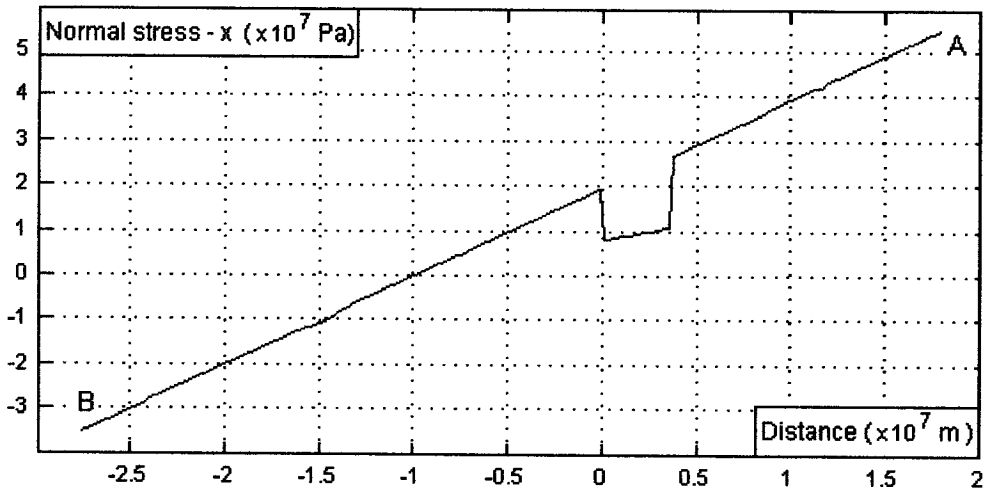

Fig.3.5. Distribution of normal stress in x-direction along a vertical line AB, shown in Fig.3.4, in sensor area

It should also be mentioned that due to the existence of the opening in the frame the distribution of stress between different branches of the sensor, is not uniform and as can be seen from Fig.3.6, the closer branches to the opening, feel more stress with respect to the farther ones. To show this phenomenon, the integral of stress in x-direction in the volume of each branch has been taken as the measure of comparison.

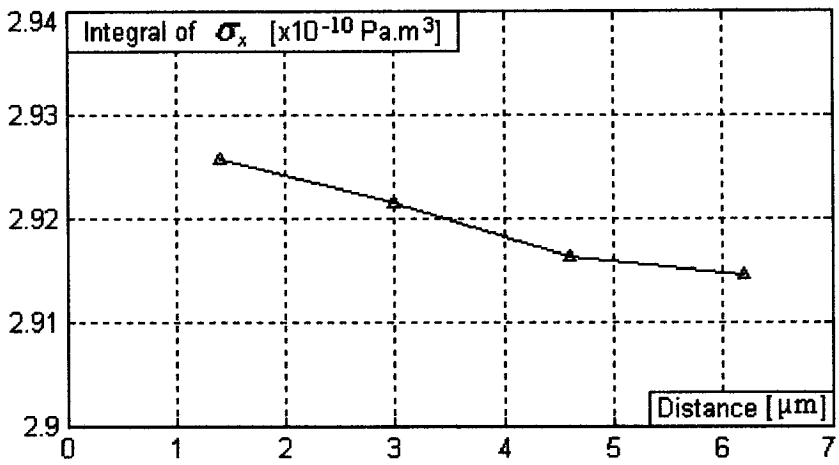

Fig.3.6. Volume integral of the average stress inside the resistor branches versus the lateral distance of the branch from the opening.

3.3 Deformation

Fig.3.7 displays the deformation of the probe (resistor length = 90 μm) under a vertical (z-direction) load of 78 nN (which is a typical force value in contact mode AFM).

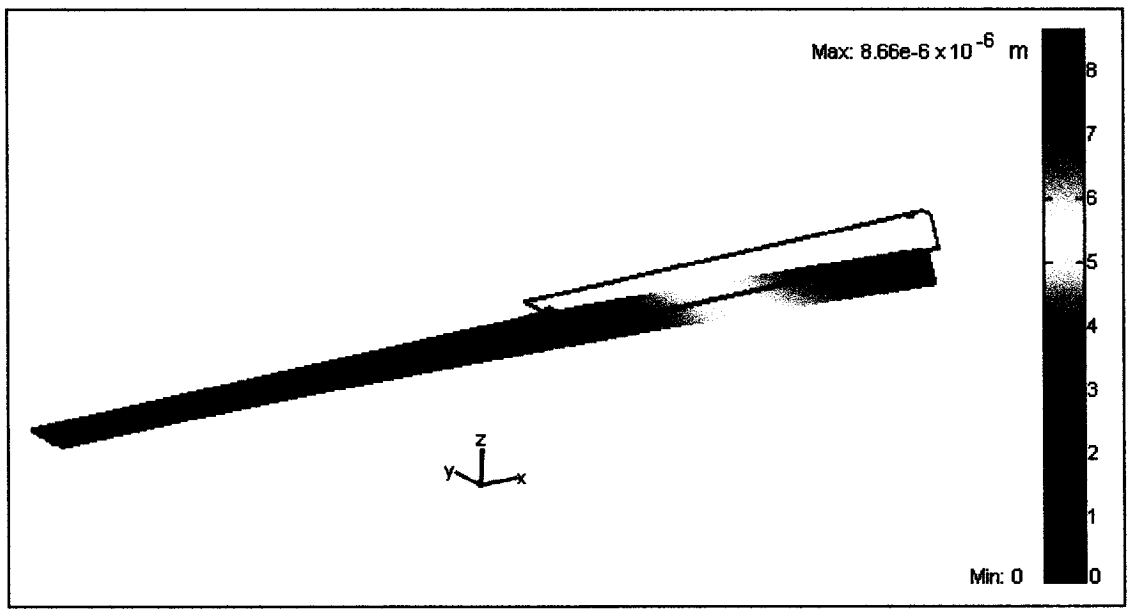

Fig.3.7. Deflection of the probe with 90 μm resistor length, due to 78 nN vertical load

Fig.3.8 displays z-direction displacement of a vertical line along the length of the probe (resistor length = 60 μm) due to 11 different equidistance forces from 0 to 78 nN.

The conformity of the curves with the predictions of simple theory of bending is appreciable in the following respects:

1. The linear relationship between the applied force and the deflection at each point.
2. The maximum curvature at the fixed end and zero curvature at the tip.
3. Zero slope at the fixed end and the maximum slope at the tip.
4. Fitting to the 3rd degree polynomial relationship between the deflection of each point and its distance from the fixed end of the beam.

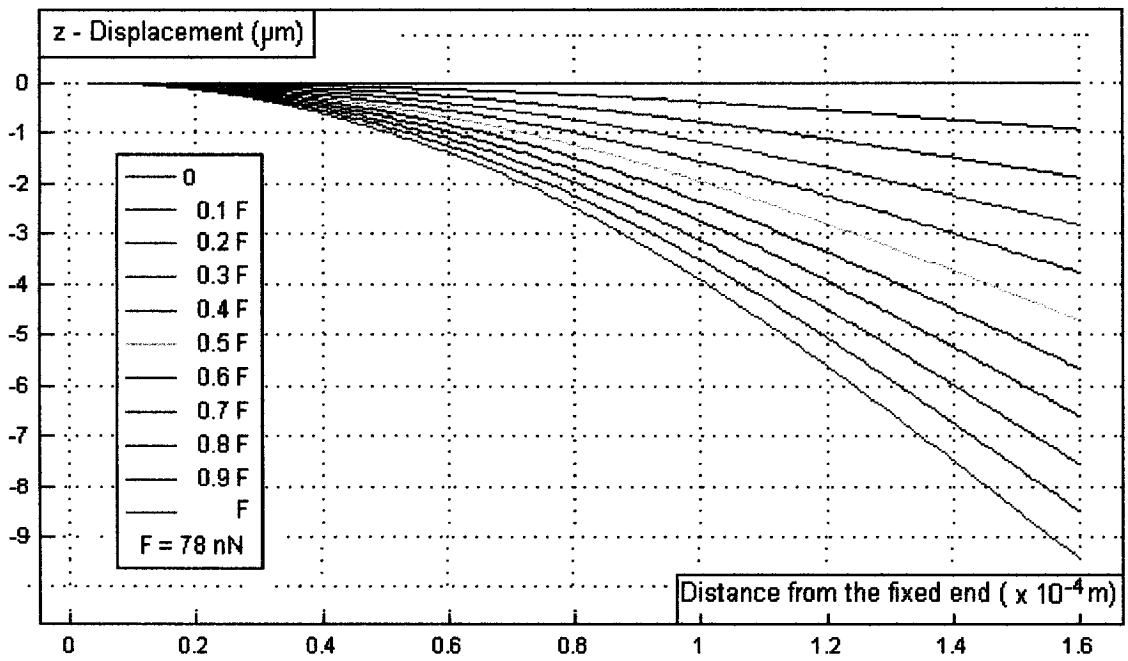

Fig.3.8. Deflection of the probe with 60 μm resistor length, due to 11 different vertical loads

3.4 Distribution of Current Density

Fig.3.9 displays the current density streamlines along with the distribution of the electric potential throughout the sensor, and Fig.3.10 is a close-up picture of the connection point between Poly2 and metallic Contact. The tendency of the streamlines to transfer their way from the polysilicon to the metal using the shortest possible path, has been shown clearly. This phenomenon, which is due to the much higher conductivity of

metal in comparison with that of Polysilicon, reduces the effective length of resistor branches.

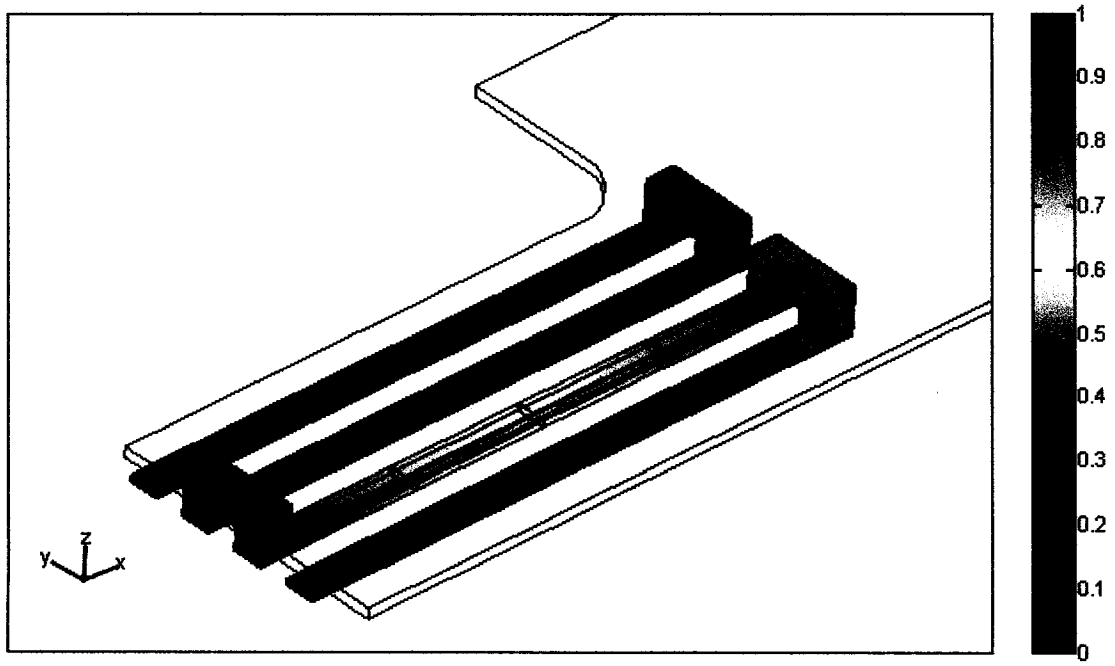

Fig.3.9. Distribution of electric potential and current density flux inside the sensor part

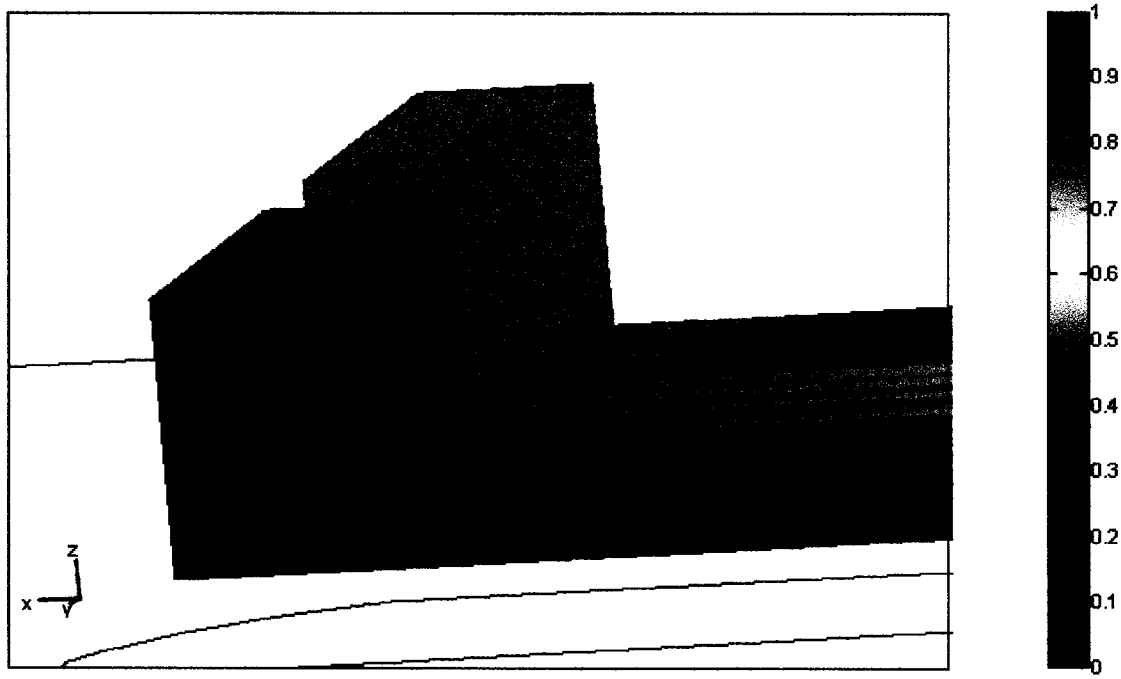

Fig.3.10. Streamlines of current density at the connection point of Poly2 and Metal

This phenomenon does not affect our study since we have mentioned the physical lengths of the resistors (from the edge of the frame to the border of Poly2 and air) wherever is applicable, regardless of this phenomenon.

3.5 Optimization in Terms of Signal to Noise Ratio (the Length of Sensor Branches)

The lower detection limit, one of the main performance factors of any sensor system, is generally defined by the signal-to-noise (S/N) ratio. The latter is mostly dependent on noise properties of a sensor gauge and an applied measurement circuit. In the proposed design, the output signal of the piezoresistive sensor is going to be measured by a Wheatstone bridge, which is typical for a great variety of sensor systems. In this chapter we analyze the output signal voltage as well as the noise voltage sensed at the terminals of the bridge, for a given typical work conditions.

For an arbitrary length of sensor branches (Let's say $L = 30\mu m$) we assume the following values:

$V = 0.7$ V, $f_1 = 1Hz$, $f_2 = 5kHz$, $\alpha_H = 10^{-3}$ [29], $F = 78nN$

where V is the supply voltage and f_1 and f_2 are the lower and upper cut-off frequencies of the filtering stage, respectively.

The reason of taking these values for the supply voltage and frequency range in working condition will be explained below.

Sheet resistance of Poly2 = 50 $\Omega/Square$

$\Rightarrow$ Resistivity of Poly2 layer = $\rho = 9 \times 10^{-4}\ \Omega.cm$

$\Rightarrow$ from simulation : Sensor resistance = Rs = 7327Ω

& change of the resistance of the sensor due to the applied force = $\Delta Rs = 27.13\Omega$

(Eq.1.9) $\Rightarrow$ Signal voltage = $Vs = 6.48\times10^{-4}V$

(Eq.1.4) $\Rightarrow$ at T =350 K : Thermal noise voltage = $\overline{V_{TN}} = 8.41\times10^{-7}V$

(Eq.2.12) $\Rightarrow$ conductivity of Poly2 = $\sigma = {}^{1}\!/_{\rho} = 1111.1(\Omega.cm)^{-1} = ep\mu_p$

Assuming $\mu_p = 60 {}^{cm^2}\!/_{V.S}$ $\Rightarrow$ dopant concentration in Poly2 = $p = 1.16\times10^{20}cm^{-3}$

Volume of the piezoresistor = $4\times(30\times0.8\times0.18) = 17.28\mu m^3 = 1.728\times10^{-11}cm^3$

The number of free carriers, N, is equal to the number of dopants inside the piezoresistor

$\Rightarrow$ $N = p\times$ Volume of the piezoresistor $= 2\times10^9$

(Eq.1.6) $\Rightarrow$ Low frequency noise voltage = $\overline{V_{LFN}} = 7.22\times10^{-7}V$

(Eq.1.10) $\Rightarrow$ $\frac{S}{N}(half-probe) = 584.46$

but all of the above values are for a half of the probe (Section 3.1) therefore for the complete probe:

$\Rightarrow$ $\frac{S}{N} = \sqrt{2}\times584.46 = 826.55$

The main question at this point is: "Is this value for S/N ratio the best possible value, and if not, under which conditions we can have a better signal to noise ratio?"

To answer this question we have to review the equations describing signal and noise voltages in the system. We answer this question in terms of different values for the sensor resistance. Since in the Wheatstone bridge based measurement system, there is an optimized fixed value for the electric current in the bridge branches (the bridge is assumed to be in equilibrium) allowing to get the maximum signal voltage at the

terminals while keeping the temperature of the sensor part in an acceptable level, we assume the same fixed current value for all different sensor resistances (the constant current mode). It can be accomplished by matching the supply voltage of the bridge for each resistor. It is also assume that all resistors in the Wheatstone bridge have the same value. Considering Eq.1.9 and Eq.1.10, we can conclude that if the value of V_{TN} and $V_{1/f}$ are equal we will have a better value for S/N than what we got in the above calculations. A small change in the supply voltage (V = $0.82V$), makes these two noise voltages equal. Therefore we fix the value of $\frac{V}{Rs} = 1.12 \times 10^{-4} A$ during our study. Fixing the value of $\frac{V}{Rs}$ makes the value of Vs to be a function of ΔRs only (Eq1.9).

On the other hand, there are two noticeable sources of noise in the system. If we fix the frequency range of the filtering stage, typically included in the electronic circuit following the bridge, then according to Eq.1.4 the thermal noise voltage will be a function of $\sqrt{Rs}$.

The low frequency noise seems to be a function of both supply voltage and N. In our study we change the value of the piezoresistor by changing the length of the resistor branches. Therefore the value of N will be a linear function of the resistor length and consequently a linear function of the resistance of the sensor.

We assumed the same current for different sensor resistances, and this assumption makes the value of V a linear function of R, as well. According to Eq.1.6 low frequency noise voltage will then be a function of $\sqrt{\frac{Rs^2}{Rs}} = \sqrt{Rs}$. Consequently the total noise voltage can be expressed as a function of $\sqrt{Rs}$ (Eq.1.10).

If we increase the length of the piezoresistor, the resistance of the sensor, Rs, will increase in a proportional way and the total noise voltage will increase proportional to $\sqrt{Rs}$. But the change of the signal voltage will be a function of ΔRs. Hence if we know the rate of change in ΔRs as a function of the resistor length, making a conclusion will become simpler.

To study the effect of change in the length of the piezoresistor branches on the relative change in the resistance and consequently the S/N ratio, we studied 11 probe geometries with different sensor lengths and the same other parameters. In each probe, the length of the rectangular opening was equal to the length of each branch of the resistor (Fig.3.11).

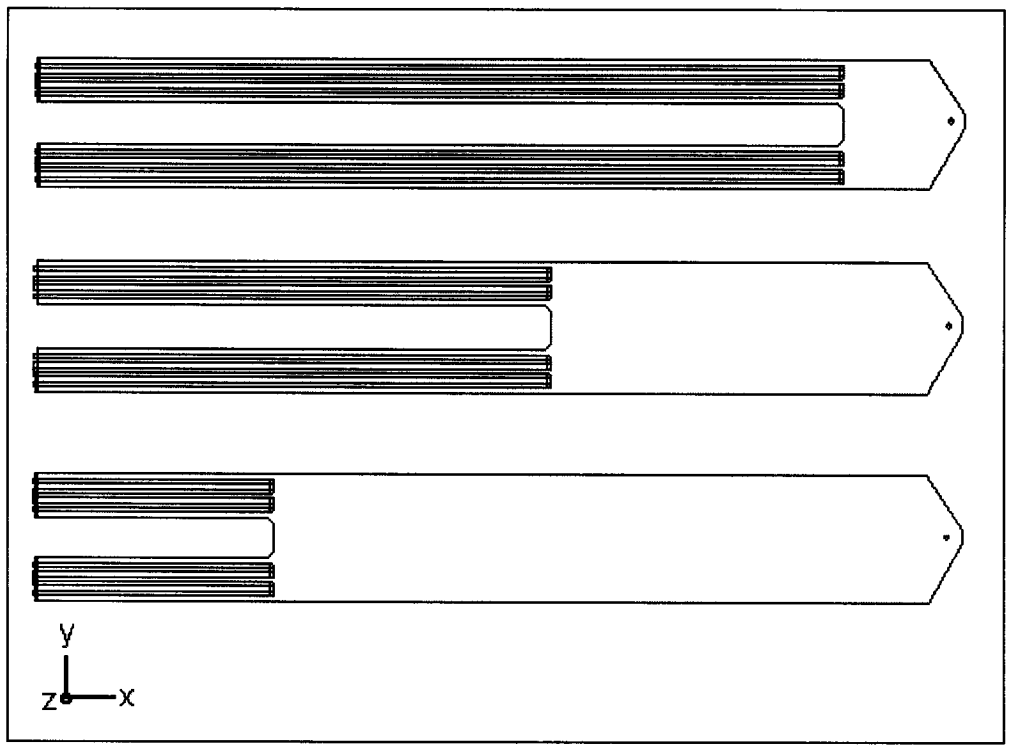

Fig.3.11. Three different probe geometries

Using computerized FEM, z-direction force equal to 78 nN was applied to the tips of the probes and the mechanical and electrical features of the probes were studied.

Fig.3.12 represents the distribution of stress along the axis of a branch of the sensor and along the frame.

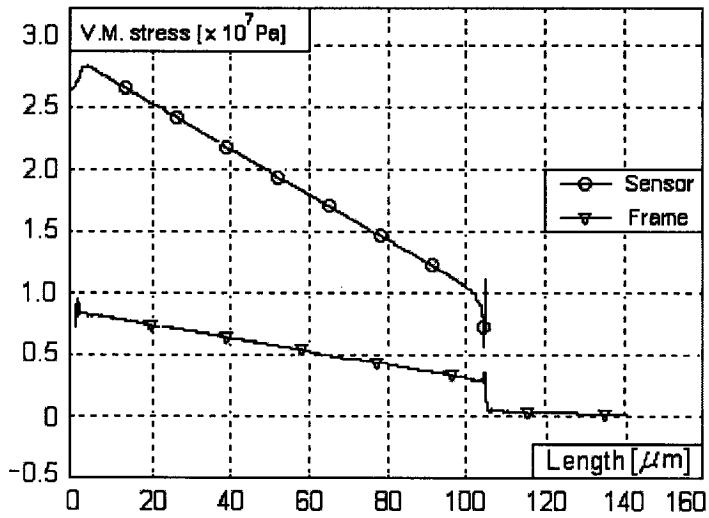

Fig.3.12. Distribution of stress along the axis of a branch of the sensor (resistor length = 105 μm) and along the frame.

The linear decrease of stress distribution along the resistor length means that increasing the sensor length does not increase change in the resistance due to stress, at the same rate, because the extended resistor parts feel less stress than their predecessors with the same length do.

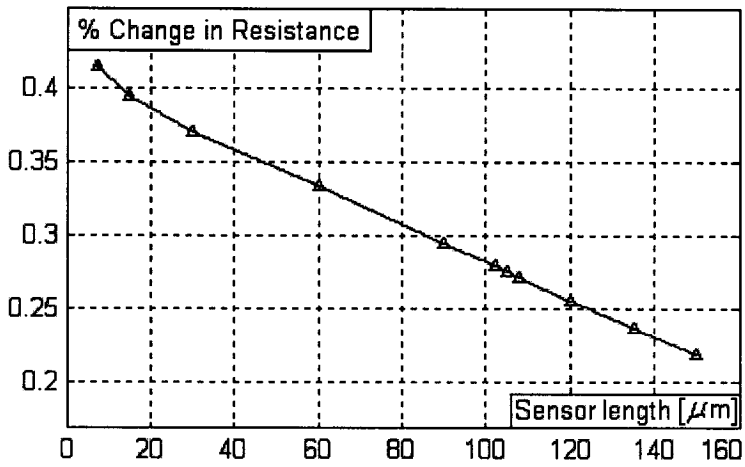

Fig.3.13. The percentage of change in resistance of the sensor for F=78 nN as a function of sensor length

The quantitative explanation of the previous discussion can be seen in Fig.3.13, in which the relative change of the resistance of the sensor ($\Delta R/R$) due to the applied force is depicted as a function of the sensor length.

Consequently, regarding to previous discussion, it can be concluded that due to the form of the distribution of stress along the sensor and the resulting ΔRs, there have to be an optimum length of sensor branches, for which the S/N ratio is maximum. Using the results of the FEM modeling of 11 different probe geometries, and following the same assumptions and the same calculation procedure, the respective values of signal and total noise voltages for different sensor lengths are computed and depicted in Fig.3.14.

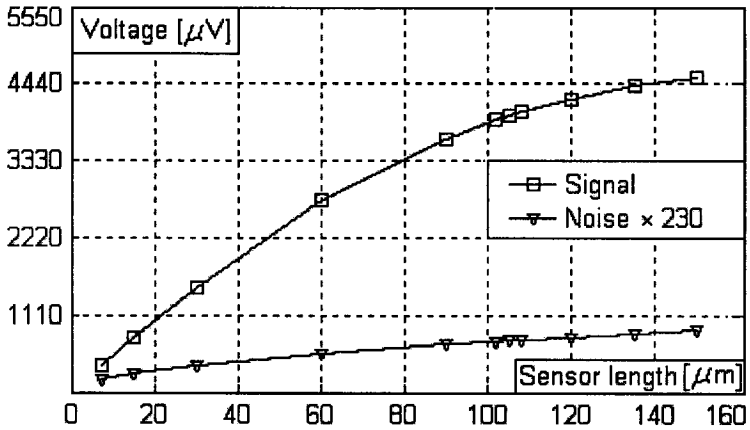

Fig.3.14. Signal and noise voltages as a function of sensor length (applied force = 78 nN)

The resulting S/N ratio is shown in Fig 3.15. It is clear from the figure that the optimum length of the sensor in terms of S/N ratio and consequently the lower detection limit, occurs at about 105 μm or at 66% of the probe length.

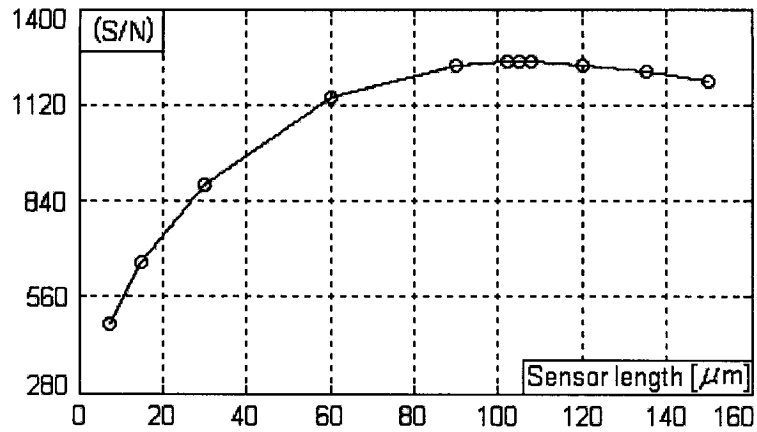

Fig.3.15. S/N ratio for different lengths of the resistor branches (applied force = 78 nN)

Hence, due to the form of stress distribution along the cantilever, there is a specific length of sensor branches, for which the maximum S/N ratio and minimum detection limit of the force can be achieved. For the taken parameters, the maximum S/N ratio equal to 1258 corresponding to the lower detection limit equal to 62 pN was calculated for the optimum length of sensor branches.

The corresponding supply voltage of the bridge for this optimum length of piezoresistor branches for the complete structure is 5.76 V.

3.6 The Effect of the Rectangular Opening

By fixing the resistor length at its optimum value (105 μm), the effect of the rectangular opening configuration on the sensitivity of the AFM probe, has been studied. For this, two other probe models were proposed and investigated. In the first model, the opening was completely eliminated. The resulted straight but narrower structure showed 7% less sensitivity than its predecessor. In the second design, the number of openings

was increased to six, as shown in Fig.3.16. The modeling proved that the sensitivity decreased by 5%. Consequently neither of these geometry changes is recommended.

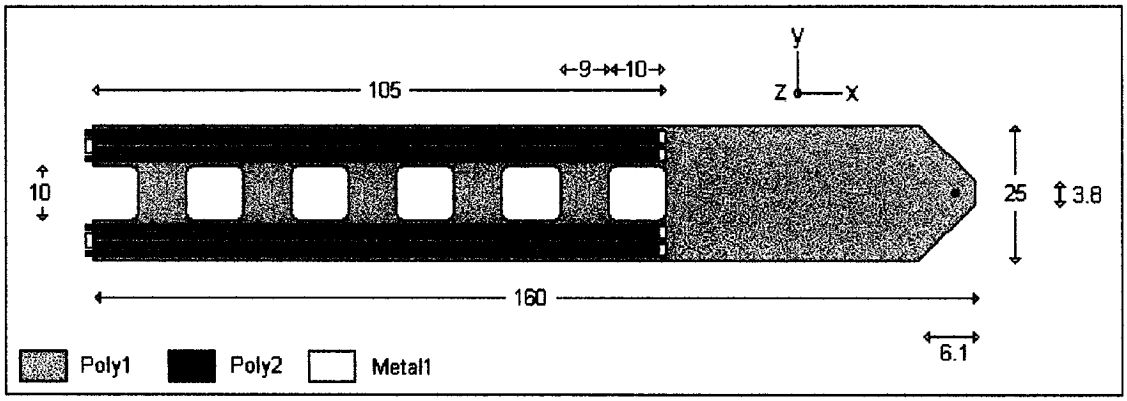

Fig.3.16. The multi-opening counterpart of the probe with the optimum resistor length

3.7 Eigenfrequencies

The eigenfrequencies of different probe geometries obtained on the basis of FEM modeling, are shown in Table.3.2. Using this table, 20482 Hz is the first eigenfrequency of the probe with optimum sensor length. This value determines the upper limit for the scanning speed, and the cut-off frequency to which the signal conditioning stage should be adjusted.

SENSOR LENGTH (MICRON)	*1.ST EIGENFREQUENCY (HZ)*	*2.ND EIGENFREQUENCY (HZ)*
7.5	15718	98330
15	16327	1.01e5
30	17462	1.04e5
60	19200	1.062e5
90	20152	1.2e5
105	20482	1.29e5
120	20848	1.36e5
150	22107	1.4e5

Table.3.2. The first and the second eigenfrequencies of the studied probes

The amount of 5 kHz used in the previous calculations of S/N ratio as the upper cut-off frequency of the filtering stage, is almost ¼ of the first natural frequency of the beam.

3.8 Optimization in Terms of Eigenfrequency

The structure shown in Fig.3.17 is proposed to increase the natural frequency of the beam with optimum sensor length. The poly-resistor branch lengths have been increased almost up to the free end of the beam. Having the metal bridges at the original location, we have the same effective length and consequently the same amount of resistance for the piezoresistors. The extended parts only increase the mechanical stiffness of the probe areas close to the free end, without noticeable affecting of the sensitivity. The modeling results showed 22170 Hz for the first eigenfrequency of the probe along with 1.2% increase in S/N ratio.

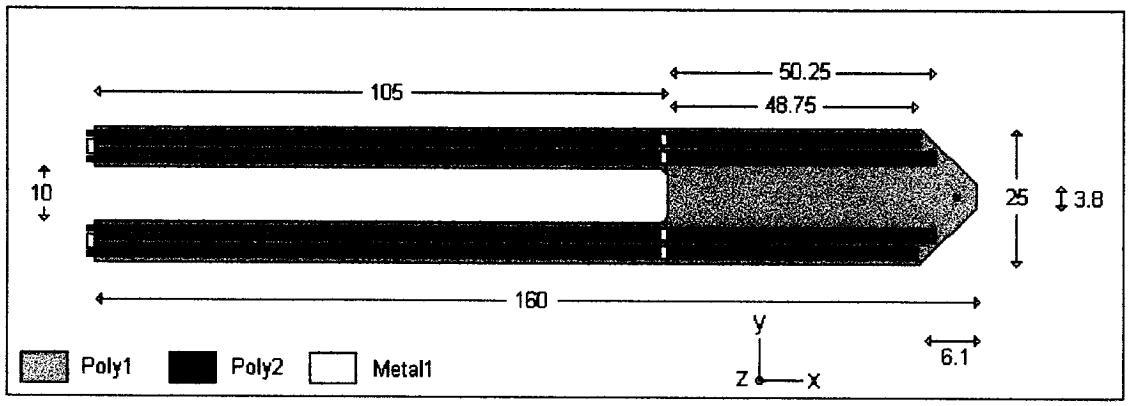

Fig.3.17. The recommended structure of the probe for increasing the eigenfrequency

3.9 Optimization in Terms of Signal to Noise Ratio (the Width and the Number of Branches)

Considering that we have fixed the length of each branch of the piezoresistor at 105 μm and $\frac{V}{Rs} = 1.12 \times 10^{-4} A$, we studied the effect of changing the width of each branch and the number of branches (that affects the total length of the piezoresistor). Because of the memory problems, modeling of this section faced some difficulties; therefore an analytical approach has been chosen for this part. If we assume that for the new configuration, the total length of the resistor and the width of each branch have been multiplied by l and w respectively, and if we assume that $l \times w$ is equal to 1, then in the y-z cross section of the beam (shown in Fig.3.3,4) the area of the Poly2 layer will remain constant and so will the second moment of area of the cross section. Therefore, according to the simple theory of bending the mechanical characteristics of the device, like the position of the neutral plane, the amount of deflection for a specific force and the stress in each point of the sensor remain the same (the amount of change in the stress, due to the distance of the branch from the opening is negligible (Fig.3.6)). Hence we can expect the same value for $\Delta R/R$ due to the same force. Therefore for the piezoresistor:

$R = \frac{\rho L}{Wd} \Rightarrow$ because the thickness of the Poly2, d, is constant : $\frac{R_2}{R_1} = \frac{l}{w}$

(Eq.1.9) $\Rightarrow \frac{Vs_2}{Vs_1} = \frac{\Delta R_2}{\Delta R_1} = \frac{R_2}{R_1} = \frac{l}{w}$

(Eq.1.4) $\Rightarrow \frac{\overline{V_{TN2}}}{\overline{V_{TN1}}} = \sqrt{\frac{R_2}{R_1}} = \sqrt{\frac{l}{w}}$

$$\frac{V_2}{V_1}=\frac{R_2}{R_1}=\frac{l}{w} \quad \text{and} \quad \frac{N_2}{N_1}=\frac{(Volume-of-the-resistor)_2}{(Volume-of-the-resistor)_2}=\frac{(LWd)_2}{(LWd)_1}=lw$$

$$\text{(Eq.1.6)} \Rightarrow \frac{\overline{V_{LFN2}}}{\overline{V_{LFN1}}}=\sqrt{\left(\frac{V_2}{V_1}\right)^2\times\left(\frac{N_1}{N_2}\right)}=\sqrt{\frac{l}{w^3}}$$

$$\text{(Eq.1.9) \& (Eq.1.10)} \Rightarrow \left(\frac{S}{N}\right)_2=\frac{\frac{l}{w}Vs_1}{\sqrt{\frac{l}{w}\overline{V_{TN1}}+\frac{l}{w^3}\overline{V_{LFN1}}}}$$

Now considering that for R_1 the values of thermal noise and low frequency noise are the same and $\left(\frac{S}{N}\right)_1=\frac{Vs_1}{\sqrt{2\overline{V_{TN1}}}}$ it can be concluded that:

$$\left(\frac{S}{N}\right)_2=\sqrt{\frac{2lw}{w^2+1}}\left(\frac{S}{N}\right)_1 \quad \Rightarrow \quad \left(\frac{S}{N}\right)_2=\sqrt{\frac{2}{w^2+1}}\left(\frac{S}{N}\right)_1 \qquad \text{(Eq.3.1)}$$

Eq.3.1 shows that to have better S/N ratio for the new resistor geometry, the value of w should be less than 1 and as small as possible. It means decreasing the width of the resistor (and increasing the length of the branch in a proportional way) leads to a better S/N ratio.

Due to the configuration of the resistors, the number of the resistor branches in each side of the opening should be an even number. On the other hand, CMOSP35 design rules sets the minimum width of the Poly2 paths equal to 0.35 μm (it is already 0.8 μm in the mentioned design). The number of branches in each side of the opening is 4, thus it can be increased to 6, 8, 10,... providing that the corresponding resistor width remains greater than 0.35 μm. Therefore the best choice for the number of branches in each side of the opening is 8, and the resistor width equal to 0.4 μm. This configuration results in

26.5% enhancement in S/N ratio. The final value of the minimum detection limit of the probe (considering all enhancements) will be 50 pN.

3.10 Target Post-Processing Steps and Anticipated Problems

CMOS 0.35μm technology allows a designer to put Polysilicon and metal layers, as well as Contacts and Vias wherever needed. However, having Oxide layers is mandatory and therefore when the proposed design is fabricated, the device is surrounded with Oxide. These superfluous Oxide layers, along with the substrate area under the device, have to be etched off in the post-processing steps to release the structure. Fig.3.18 displays a sketch of the layers in the proposed device after fabrication. As it can be computed from the information given in Table.3.1 the thickness of the Oxide on top of the device is 3428 nm. Also the thickness of the Oxide on top of the substrate and the rectangular opening is 3645 nm. These SiO_2 layers along with the 180 nm Oxide layer beneath the frame (Poly1) should be all etched away and only the intermediate SiO_2 layer between Poly1 and Poly2 should remain untouched.

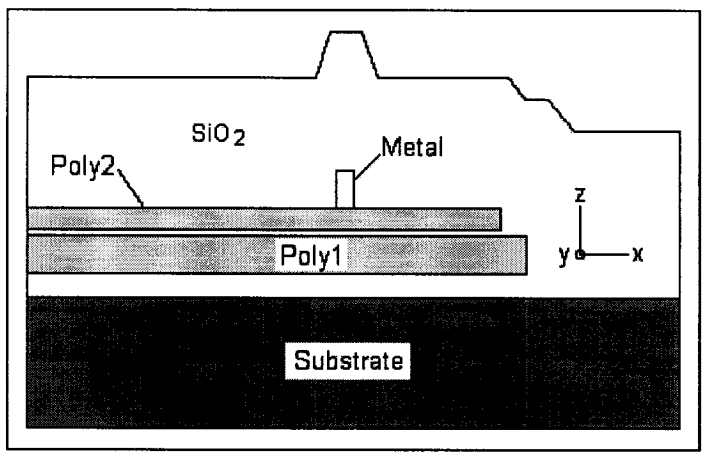

Fig.3.18. Schematic cross section of fabricated device before post-processing (the dimensions are not scaled)

A four–stage masked chemical etching has been predicted to release the device (the required masks for steps 1 & 2 have been shown in Fig.3.19):

Step 1: Using mask-1, 3248 nm of Oxide will be eliminated in buffered-HF. After step1 we still have 180 nm of Oxide on top of the device areas and 397 nm Oxide on top of the substrate and the opening.

Step 2: Using Mask2, 397 nm of Oxide on the substrate and the opening will be eliminated in buffered-HF to reach the substrate in these areas. Considering the isotropic under-etch, there should be still, 180 nm Oxide surrounding the device from all directions except the fixed end of the cantilever.

Step 3: The substrate is etched away in TMAH to make the required cavity and release the device (surrounded by 180 nm Oxide) from the substrate.

Step 4: the surrounding Oxide will be eliminated in buffered-HF to reach the surface of the probe from each direction. The timing in this step is critical because over-etching can damage the intermediate Oxide layer between Poly1 and Poly2.

Using different masks for step 3 and 4 may also be necessary to protect the Pads, and prevent undesired under-etch. Fig.3.19 shows a schematic of the first two steps of post-processing. In this figure m1 and m2 are the distances between the edge of the mask-1 and mask-2 and the corresponding borders in the device or cavity, and are about 3240 nm and 577 nm respectively.

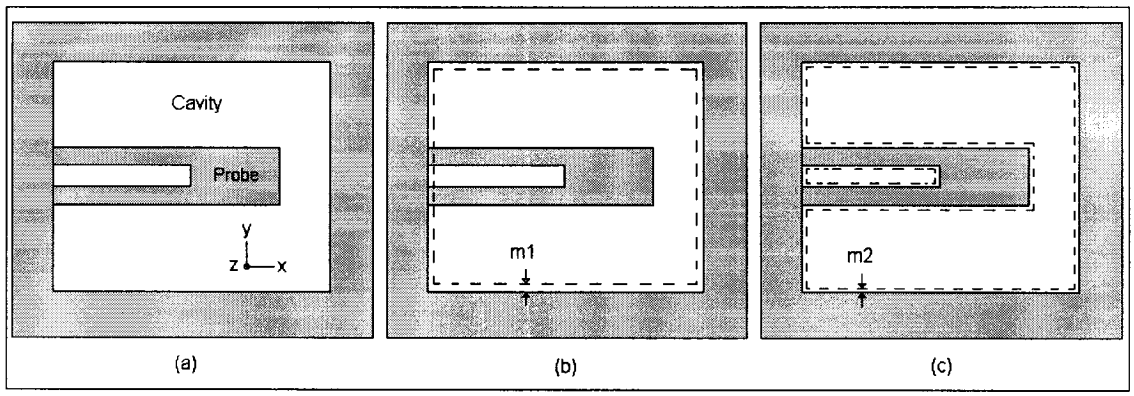

Fig.3.19. Schematics of (a) the final released device (b) borders of mask-1 (c) borders of mask-2 (The dimensions are not in proportion)

There are some minor CMOS 0.35μm technology design rules violations in the recommended device (like the dimensions of the Contact parts), which are generally accepted by manufacturers as intentional. Therefore no problem is expected in the manufacturing phase.

But in the releasing step, etching all oxide layers except the intermediate layer between the polys, is a very deliberate process, and therefore remaining of some oxides in the corners, or conversely over-etching of the layer, is possible. In each case the sensitivity of the device would be negatively affected.

Also, the surface of the frame will be covered by a very thin native oxide layer, after release, that does not considerably affect the mechanical structure of the probe.

CHAPTER 4 CONCLUSIONS AND FUTURE WORKS

4.1 Contribution and Conclusions

The goal of this work was to propose an optimized AFM probe structure that can be fabricated using standard CMOS 0.35μm technology and utilizing a multistage masked post-micromachining process.

An effective structure for an AFM cantilever with integrated piezoresistive sensor, based on CMOS 0.35μm technology has been proposed. Among the large number of possible combinations from the 12-layer stack of CMOS 0.35μm technology, a seemingly best combination of the layers for different parts of the probe was selected. To avoid the drawback of the transverse parts of conventional meander-like piezoresistors, a bridge-like structure was proposed to replace the transverse parts of the piezoresistor.

The advantages of the design are high sensitivity and low detection limit as well as susceptibility to passivating of the sensor part using soft organic materials to prevent degradation of the sensor characteristics. The recommended design also exhibits the least possible residual stress in its structure.

By studying the mathematical equations governing the mechanical and electrical behavior of the probe and by using the results obtained from finite element method analysis of the design, the optimum sensor and frame parameters and geometry, in terms of S/N ratio (and consequently minimum detection limit) as well as eigenfrequency, was recommended and approved.

Using a 5 KHz band-pass filter in the conditioning circuit, the minimum detection limit of the final proposed design is 50 pN and its first eigenfrequency is above 22 kHz.

These characteristics make the recommended probe a qualified candidate for Contact and Tapping mode AFM systems.

4.2 Related Publications

Mehran Hosseini, Victor Rossokhaty, Mojtaba Kahrizi, "Design and optimization of an AFM probe, based on piezoresistance effect", to be published in the proceedings of IEEE CCECE 2005

4.3 Future Works

Fabrication of the proposed probe followed by characterization to verify the theoretical parameters, can be the next step for this work. Some actuation mechanisms should be considered in the fabricated device to make it testable. Although adding an actuation mechanism to the design may cause some necessary changes in the structure, it should not considerably affect the sensitivity of the recommended probe.

Design of the measurement circuits as well as the conditioning and processing stages and integration of them along with the probe in a single chip can also be considered.

References

[1] H. J. Mamin, B. D. Terris, L. S. Fan, S. Hoen, R. C. Barrett, and D. Rugar, "High-density data storage using proximal probe techniques," IBM Journal of Research and Development, vol. 39, no. 6, pp. 681–699, November,1995

[2] S. Hosaka, H. Koyanagi, and A. Kikukawa, "Nanometer recording on graphite and Si substrate using an atomic force microscope in air," Jpn. J. Appl. Phys., vol. 32, pp. L464–L467, March, 1993

[3] George Juraj Stein, "Some Recent Development in Acceleration Sensors," Measurement Science Review, vol. 1, no. 1, pp. 183-186, 2001

[4] V. Beroulle, Y. Bertrand, L. Latorre, P. Nouet, "Evaluation of the Oscillation-based Test Methodology for Micro-Electro-Mechanical Systems," Proceedings of 20th IEEE, VLSI Test Symposium, 2002

[5] Robert D. White, Karl Grosh, "Design and Characterization of a MEMS Piezoresistive Cochlear-Like Acoustic Sensor," Proceedings of IMECE'02 2002 ASME International Mechanical Engineering Congress and Exposition, New Orleans, Louisiana, IMECE2002-33309, November, 2002

[6] C. Bergaud, E. Cocheteau, L. Bary, R. Plana, B. Belier, "Formation of Implanted Piezoresistors Under 100-nm Thick for NanoElectromechanical Systems," Proceedings of the Fifteenth IEEE International Conference on Micro Electro Mechanical Systems, pp.360-363, January, 2002

[7] Chia-Yen Lee, Gwo-Bin Lee, "MEMS-based Humidity Sensors with Integrated Temperature Sensors for Signal Drift Compensation," IEEE Sensors, Toronto, Canada, October, 2003

[8] VanLandingham, M.R., S.H. McKnight, G.R. Palmese, J.R. Elings, X. Huang, T.A. Bogetti, R.F. Eduljee, and J.W. Gillespie, "Nanoscale Indentation of Polymer Systems Using the Atomic Force Microscopy," J. Adhesion, vol. 64, 1997

[9] Strausser, Yale E., Schroth, Michael, Sweeney, John J., "Characterization of the Low-Pressure Chemical Vapor Deposition Grown Rugged Polysilicon Surface Using Atomic Force Microscopy," J. Vac. Sci. Technol.,vol. 15, Issue 3, pp.1007-1013, May, 1997

[10] B. D. Terris, R. C. Barrett, "Data storage in NOS: Lifetime and carrier-to-noise measurements," IEEE Trans. Electron Devices, vol. 42, pp. 944–949, May, 1995

[11] K. Yano et al., "Information storage using conductance change of Langmuir – Blodgett film and atomic force microscope/scanning tunneling microscope," J. Vac. Sci. Technol. B, vol. 14, pp. 1353–1355, March/April, 1996

[12] R. Overneyand E. Meyer, "Tribological Investigations Using Friction Force Microscopy," MRS Bulletin, vol. 18, no. 5, pp. 26-34, 1993

[13] William P. King, Thomas W. Kenny, Kenneth E. Goodson, Graham L. W. Cross, Michel Despont, Urs T. Dürig, Hugo Rothuizen, Gerd Binnig, and Peter Vettiger, "Design of Atomic Force Microscope Cantilevers for Combined Thermomechanical Writing and Thermal Reading in Array Operation," Journal of Microelectromechanicla Systems, vol. 11, no. 6, pp. 765-774, December, 2002

[14] Revenko I., "Probing the Life Sciences with Atomic Force Microscopy," Proceedings of 1st Symposium in Micro- and Nanostructures of Biological Systems, pp. 1–51, October 4–5, 2000

[15] Magonov S.N., "Visualization of Polymers at Surfaces and Interfaces with Atomic Force Microscopy," HANDBOOK OF SURFACES AND INTERFACES OF MATERIALS. Vol. 2, ed. H.R. Nalwa, Academic Press, New York, 2001

[16] Shakesheff, K.M., M.C. Davies, C.J. Roberts, S.J.B. Tendler, P.M. Williams, "The Role of Scanning Probe Microscopy in Drug Delivery Research," Crit. Rev. Therap. Drug Carr. Syst., vol. 13, 1996

[17] Binnig, G., C.F. Quate, and Ch. Gerber, "Atomic Force Microscope," Phys. Rev. Lett., vol. 56, pp. 930-933, March , 1986

[18] Robert P. Ried, H. Jonathon Mamin, Bruce D. Terris, Long-Sheng Fan, and Daniel Rugar, "6-MHz 2-N/m Piezoresistive Atomic-Force-Microscope Cantilevers with INCISIVE Tips," Journal of Microelectromechanical Systems, vol. 6, no. 4, pp. 294-302, December, 1997

[19] J. Thaysen, A. Boisen, O. Hansen and S. Bouwstra. "AFM probe with piezoresistive read-out and highly symmetrical wheatstone bridge arrangement," Proceedings of the 10th International Conference on Solid-State Sensors and Actuators, The Institute of Electrical Engineers of Japan, Sendai, Japan, pp.1852-1855, June, 1999

[20] B. Gotsmann , B. Anczykowski, C. Seidel, H. Fuchs, "Determination of tip–sample interaction forces from measured dynamic force spectroscopy curves," Applied Surface Science, vol. 140 , pp. 314–319, 1999

[21] Hong-Qiang Li, "Atomic Force Microscopy" Advanced Surface Microscopy, Inc. http://www.asmicro.com/default.htm

[22] Ivo W. Rangelow, "Scanning Probe Microsystems," Proceedinds of the Third International EuroConference on Advanced Semiconductor Devices and Microsystems ASDAM 2000, pp. 71-80, 2000

[23] P. G. Datskos, T. Thundat, Nickolay V. Lavrik, "Micro and Nanocantilever Sensors," Encyclopedia of Nanoscience and Nanotechnology, Edited by H. S. Nalwa, American Scientific Publishers, Fairfield, NJ, 2003

[24] D. W. Lee, Takahito Ono, Masayoshi Esashi, "Cantilever with integrated resonator for application of scanning probe microscope," Sensors and Actuators A, vol. 83, pp. 11-16, May, 2000

[25] Y.S. Kim, Hyo-Jin Nam, Seong-Moon Cho, Jae-Wan Hong, Dong-Chan Kim, Jong U.Bu , "PZT cantilever array integrated with piezoresistive sensor for high speed parallel operation of AFM," Sensors and Actuators A, vol. 103, pp. 122-129, 2003

[26] D. Sarid, SCANNING FORCE MICROSCOPY WITH APPLICATIONS TO ELECTRIC, MAGNETIC, AND ATOMIC FORCES. Oxford University Press, New York, 1991

[27] E. A. Wachter, T. Thundat, P. G. Datskos, P. I. Oden, S. L. Sharp, and R. J. Warmack, "Remote Optical Detection Using Microcantilevers," Review of Scientific Instruments, vol. 67, Issue 10, pp. 3434-3439, October, 1996

[28] "Atomic Force Microscopy" http://www.pace.leeds.ac.uk/labs/afm.htm

[29] F.N. Hooge, "1/f Noise Sources," IEEE Transactions on Electron Devices, vol. 41, no. 11, pp. 1926-1935, November, 1994

[30] Melih Papila, Raphael T. Haftka, Toshikazu Nishida and Mark Sheplak, "Piezoresistive microphone design Pareto optimization: tradeoff between sensitivity and

noise floor," Proceedings of 44th AIAA/ASME/ASCE/AHS/ASC Structures, Structural Dynamics, and Materials Conference, Norfolk, Virginia, April 7-10, 2003

[31] J. Thaysen, A. D. Yal¸ cinkaya, P. Vettiger and A. Menon, "Polymer-based stress sensor with integrated readout," J. Phys. D: Appl. Phys., vol. 35, pp. 2698–2703, 2002

[32] Naushad Hossain, J. W. Ju, Brett Warneke, Kristofer S. J. Pister, "Characterization of the Young's Modulus of CMOS Thin Films," The American Society for Testing and Materials, 2001

[33] F. Sandoval-Ibarra, J. Esteve, and E. Gutiérrez-Domínguez, "Stress in Thin Films: Analysis of SI3N4/ AL Microstructures for sensor Applications," Instrumentation and Development, vol. 4, no. 3, pp.3-5, 2000

[34] Gary K. Fedder, "Microelectromechanical Fabrication for On-Chip Data Storage," CHIPS Open House, May, 2001

[35] Hernan A. Rueda, "Modeling of Mechanical Stress in Silicon Isolation Technology and its Influence on Device Characteristics," Ph.D. Thesis, University of Florida, 1999

[36] P.J. French, "Polysilicon: a versatile material for Microsystems," Sensors and Actuators A, vol. 99, pp. 3-12, April, 2002

[37] Nathan A. Dotson, Peter T. Kim and Andrew Mason, "Low Cost MEMS Processing Techniques," Proceedings of the 2004 ASEE/NCS Spring Conference, American Society for Engineering Education, April 1-3, 2004

[38] COMSOL Inc., FEMLAB Documents

[39] S. M. Sze, SEMICONDUCTOR SENSORS. J. Wiley, New York, 1994

[40] Fredrik Creemer and Paddy French, "The Piezojunction Effect in Silicon and its Applications to Sensors and Circuits" Proceedings of the SeSens workshop, December, 2000

[41] E. J. Hearn, MECHANICS OF MATERIALS. Butterworth Heinemann, Oxford, 1997

[42] A. A. Shabana, THEORY OF VIBRATION. Springer-Verlag, New York, 1991

[43] Donald A. Neaman, SEMICONDUCTOR PHYSICS AND DEVICES. McGraw-Hill, 2003

[44] Ferdinand Pierre Beer, MECHANICS OF MATERIALS. McGraw-Hill, London, 1992

[45] Charlot et al. "An Integrated MEMS Fingerprint Sensor," to be published in IEEE JMEMS

[46] Chang Liu, Y.Bar-Cohen, "Scaling Laws of Microactuators and potential applications of Electroactive Polymers in MEMS," Proceedings of SPIE's 6th Symposium, Newport Beach, CA, March, 1999

[47] V.A. Gridchin et al., "Piezoresistive properties of polysilicon films," Sensors and Actuators A, vol. 49, no. 1-2, pp. 67-72, 1995

[48] S. Gautsch, T. Akiyama, R. Imer, N. F. de Rooij, U. Staufer, Ph. Niedermann, L. Howald, D. Brandlin, A. Tonin, H. R. Hidber and W. T. Pike, "Measurement of quartz particles by means of an atomic force microscope for planetary exploration," Surface and Interface Analysis, vol. 33, Issue 2, pp.163–167, February, 2002

[49] Tai-Ran Hsu, MEMS AND MICROSYSTEMS DESIGN AND MANUFACTURING. McGraw-Hill, 2002

[50] Russell A. Lawton, Gisela Lin, Joanne Wellman, Leslie M. Phinney, Jose Uribe, Edward Griffith, Ingrid De Wolf, Eric Lawrence, "Micro Nano Technology Visualization (MNTV) of Micromachined MEMS Polysilicon Structures," Jet Propulsion Laboratory, California Institute of Technology 4800 Oak Grove Drive, Pasadena, California 91109-8099

[51] Ralf Brederlow, Werner weber, Claus dahl, doris Schmitt-Landsiedel, Roland Thewes, "Low frequency Noise of Integrated Poly-Silicon Resuistors," IEEE Transaction on Electron Devices, vol. 48, no. 6, June, 2001

[52] M.J.Deen, S.Rumyantsev, and J.Orchard-Webb, "Low Frequency Noise in Heavily Doped Polysilicon Thin Film resistors," J. of Vac. Sci. & Tech. B: Microelectronics and Nanometer Structures, vol. 16, Issue 4, pp. 1881-1884, July, 1998

[53] Kent H. Lundberg, "Noise Sources in Bulk CMOS," Kent Lundberg, 2002

[54] P. Russell, D. Batchelor, J. Thornton, "SEM and AFM: Complementary Techniques for High Resolution Surface Investigations," Vecco Metrology Group, www.veeco.com

[55] Tzv. Ivanov , T. Gotszalk , T. Sulzbach , I. Chakarov , I.W. Rangelow, "AFM cantilever with ultra-thin transistor-channel piezoresistor: quantum confinement," Microelectronic Engineering, vol. 67–68, pp. 534–541, June 2003

[56] J.A. Harley, T. W. Kenny, "1/f noise considerations for the design and process optimization of piezoresistive cantilevers," Journal of Microelectromechanical Systems, vol. 9, Issue 2, pp. 226-235, June, 2000

Appendix A - Material properties

Table.A.1 shows the mechanical and electrical characteristics of the materials used in the device structure [45,47,49].

Material	Young's Modulus (Pa)	Poisson's Ratio	Density (kg/m^3)	Conductivity $(/\Omega.m)$	Π11 (*)	Π12 (*)	Π44 (*)
Polysilicon	1.7×10^{11}	0.23	2330	1.11×10^{5}	-13	7.6	0.5
Metal	7×10^{10}	0.35	2710	3.16×10^{7}	0	0	0
SiO_2	7×10^{10}	0.17	2270	0	0	0	0

Table.A.1. Mechanical and electrical properties of the utilized materials $(* = 10^{-11} Pa^{-1})$

Appendix - B Description of a Fabricated Test Device

A test device was also designed and fabricated besides the recommended design, to experimentally measure the piezoresistive coefficients of Poly2 layer in CMOSP35 technology and to evaluate the precision of the modeling process.

To make the fabricated device testable using the available equipment, some actuation mechanisms had to be predicted and integrated into the structure of the test device, therefore the test device structure was different from that of the recommended design.

Two types of thermal actuators as well as an electromagnetic one was predicted and designed to excite the test probe. In thermal actuation mechanisms, a structure composed of Poly1 as the warm plate and Oxide and Metal2 as the cold plate, was used to vertically deflect the tip of the probe. Current passes only through Poly1 layer and due to the generated heat and the resulted expansion of this layer, a downward deflection of the bridge is produced and pulls the free end of the probe downward. Fig.B.1 Displays one of the combinations of the probe and the thermal actuator and Fig.B.2. is a sketch of this actuation method.

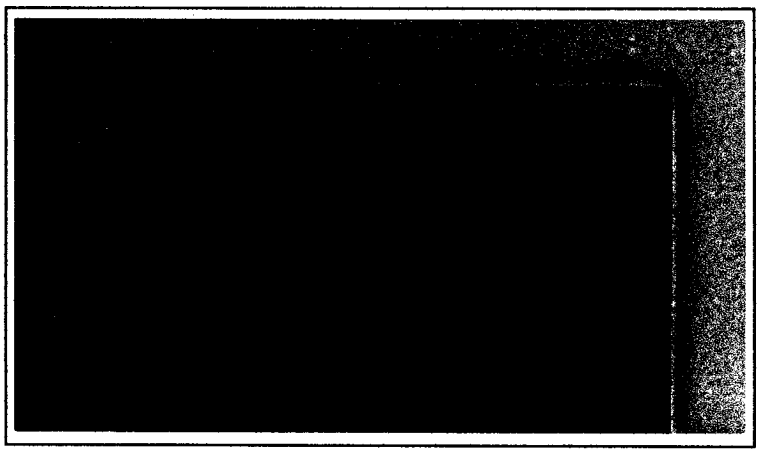

Fig.B.1. One combination of the probe and a thermal actuator

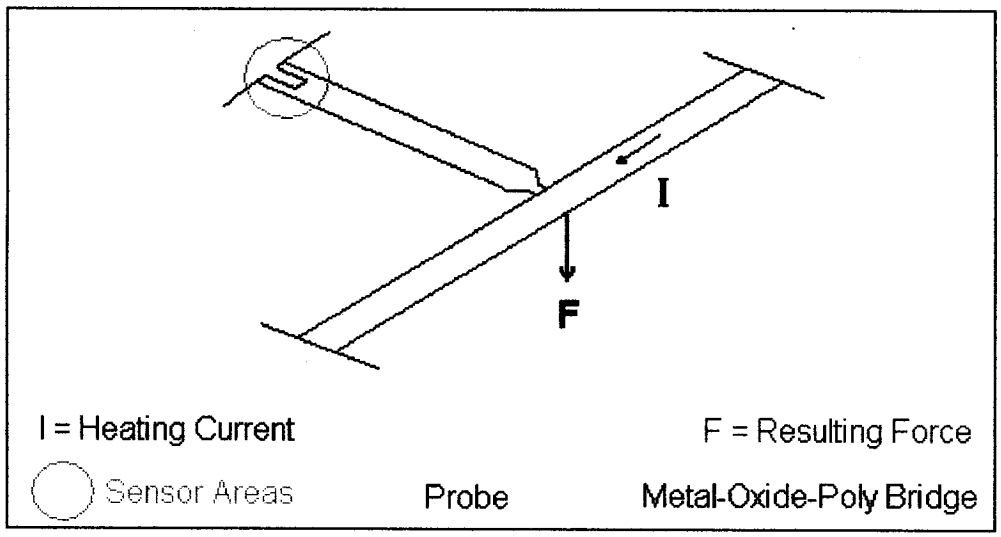

Fig.B.2. A perspective sketch of the combination of the probe and a thermal actuator

The combination of the probe and its electromagnetic actuator has been shown in Fig.B.3. In this type of actuation, a path made of Metal1, containing two parallel probes and a connecting bridge was built to provide the actuation current path. Applying a parallel magnetic field, results in a vertical force to the current path (perpendicular to the chip plane) and this vertical force is transformed to the probes in each side of the bridge..

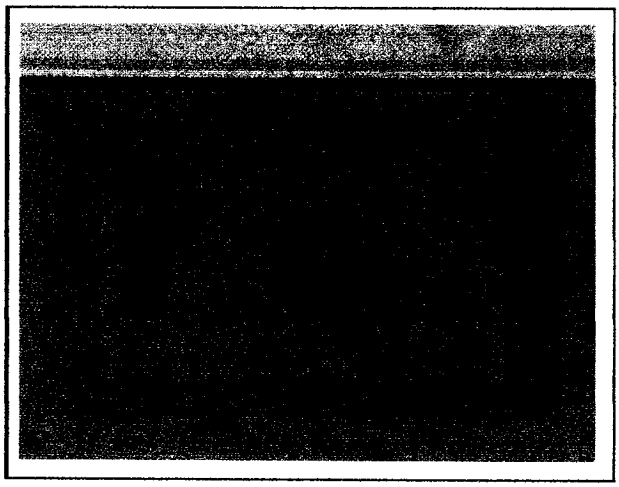

Fig.B.3. The combination of the probe and electromagnetic actuator

Fig.B.4. demonstrates a perspective sketch of the this combination of probes and actuation mechanism.

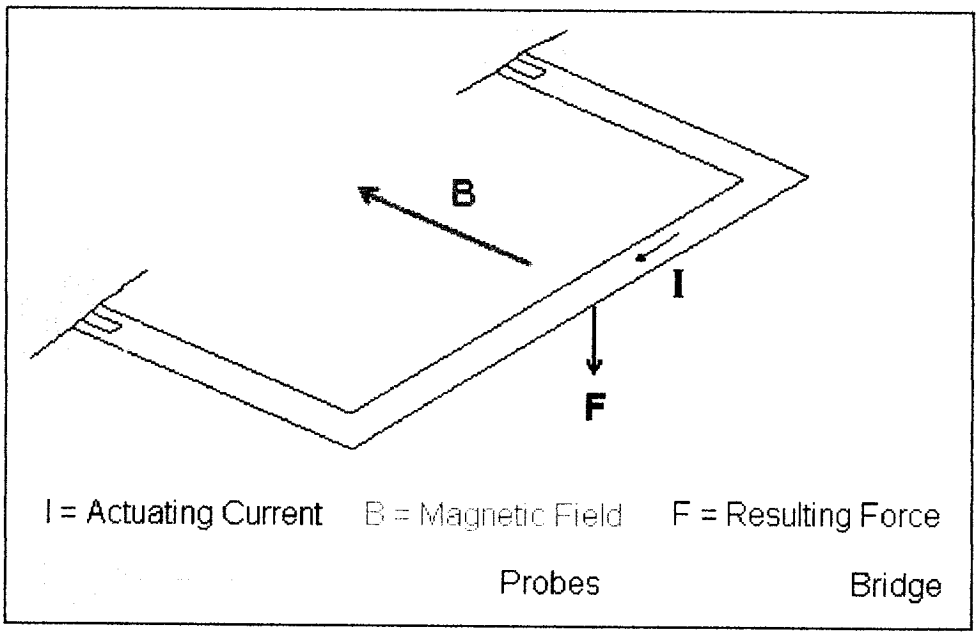

Fig.B.4. A perspective sketch of the combination of the probes and electromagnetic actuator

A four-stage masked post micro-machining process similar to that of the recommended design was considered for releasing the test device structure and the

required masks (Fig.B.5) was also designed and fabricated. Fig.B.6 displays a top-view photograph of the complete fabricated chip.

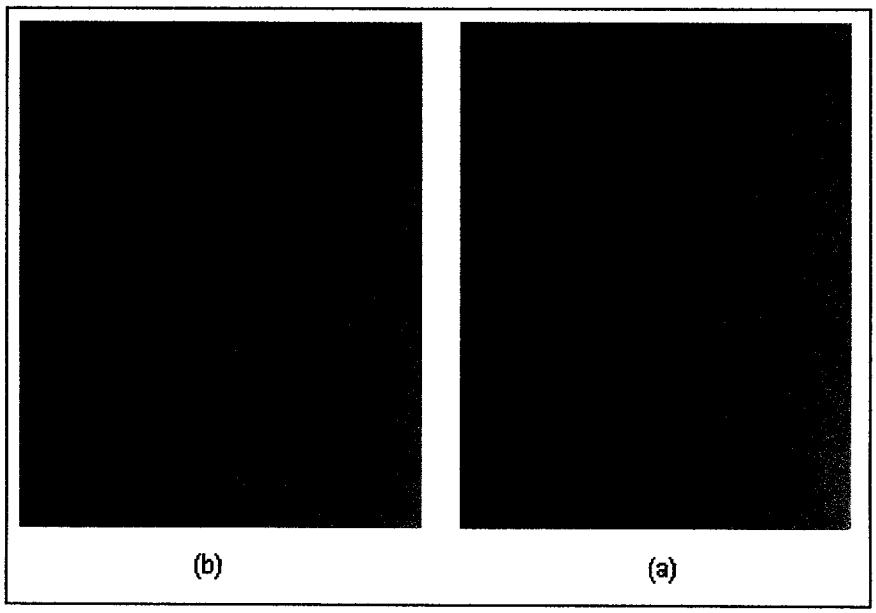

Fig.B.5. (a) first mask (b) second mask

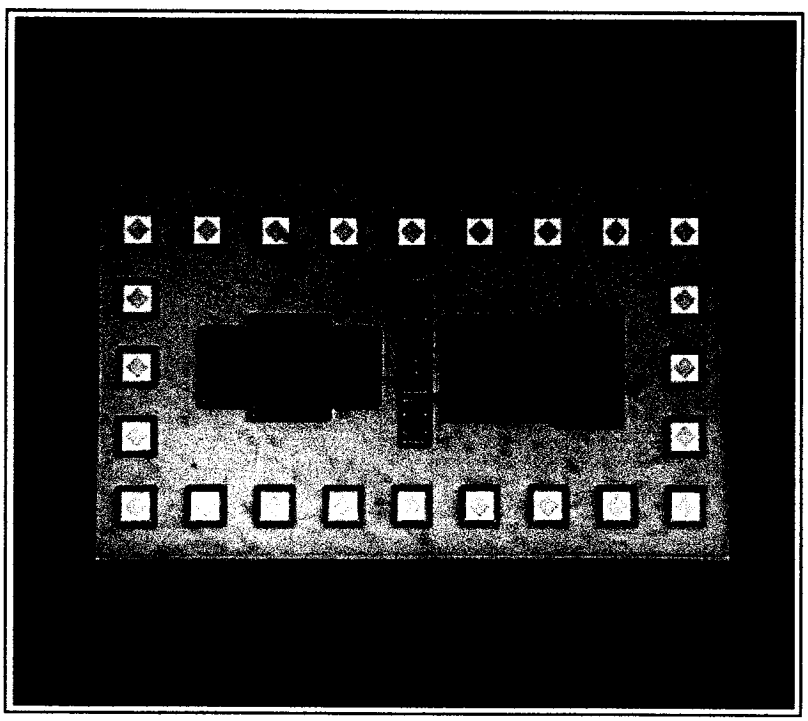

Fig.B.6. Top view of the fabricated chip

Unfortunately due to the delays in the fabrication of the device and the masks, as well as some equipment problems, the characterization of the fabricated test device was not possible at the time of thesis submission.

The following paragraphs contain the modeling results (expected) of the fabricated test device

Fig.B.7 shows a top-view sketch of test probe and Fig.B.8 highlights the composed layers in the sensor part of the probe.

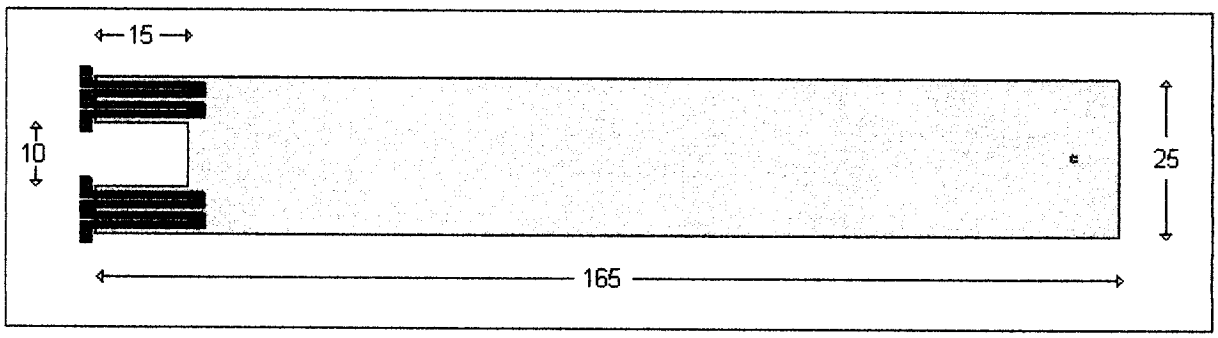

Fig.B.7. Top view of the test probe (The dimensions are in μm).

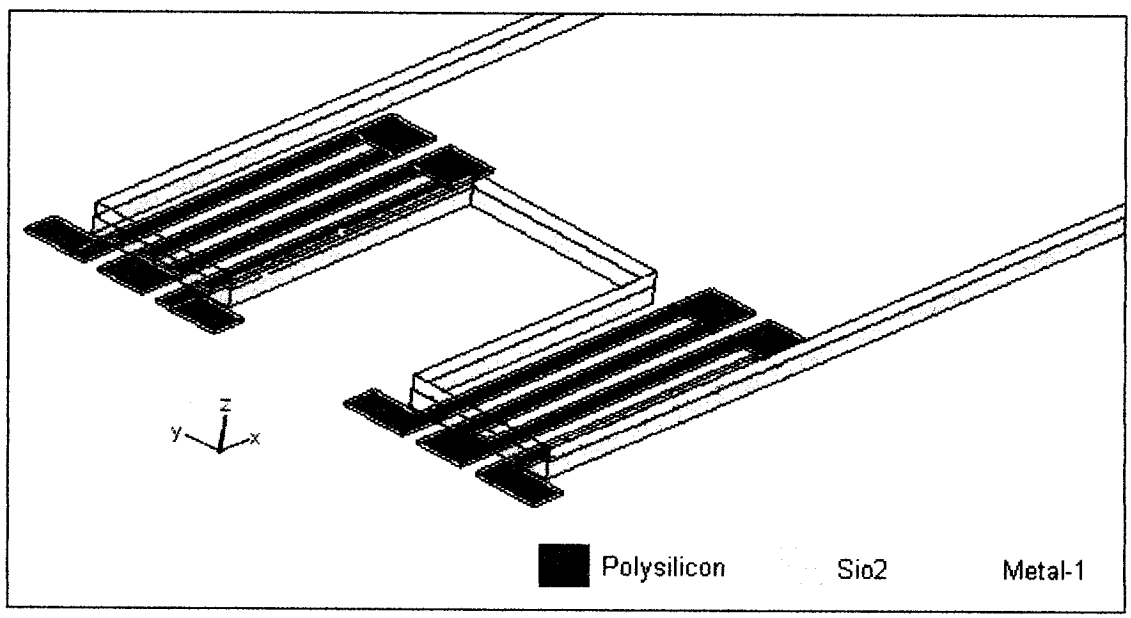

Fig.B.8. Perspective view of the sensor parts of the test probe.

The frame is composed of Oxide layers at the bottom and Metal1 layer on the top. The sensor device is located inside the Oxide layer and is made of Polysilicon (Poly2).

Deformation

The analysis was made with 11 force steps from 0 to $0.785\mu N$. The maximum deflection (at the tip) due to the applied load was $2.69\mu m$. Fig.B.9 shows the deformation along the length of the probe for 11 equidistance load steps. From the figure the linear relationship between the exerted force and the resulted deflection is apparent.

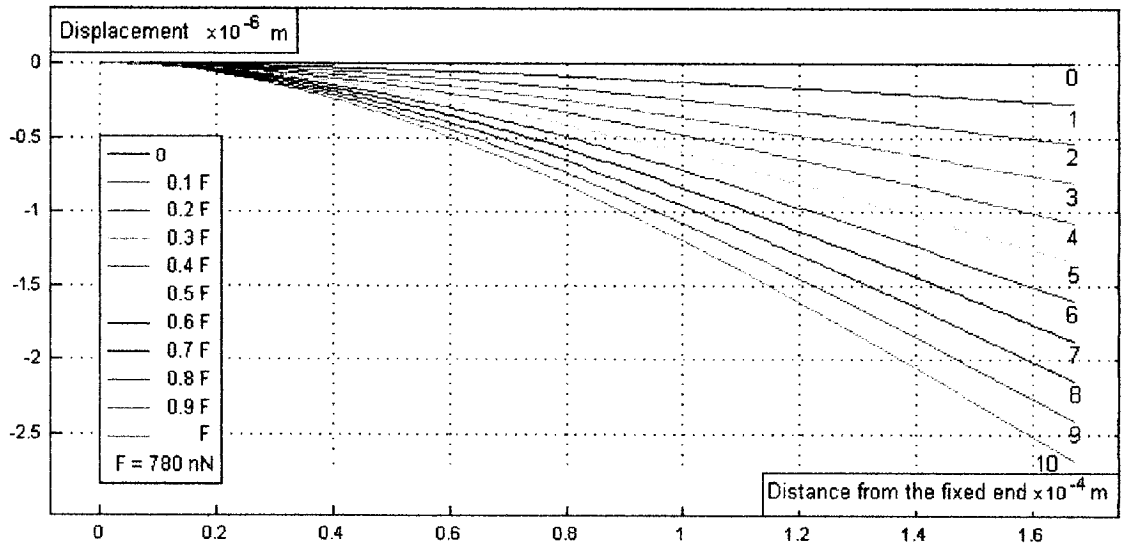

Fig.B.9. Deflection along the beam for 11 equidistance load steps.

Distribution of stress

One of the design considerations for proble-1 was setting the sensor part in the most stressed area. And this had to be verified after simulation. Fig.B.10 shows the distribution of stress along the length of the beam.

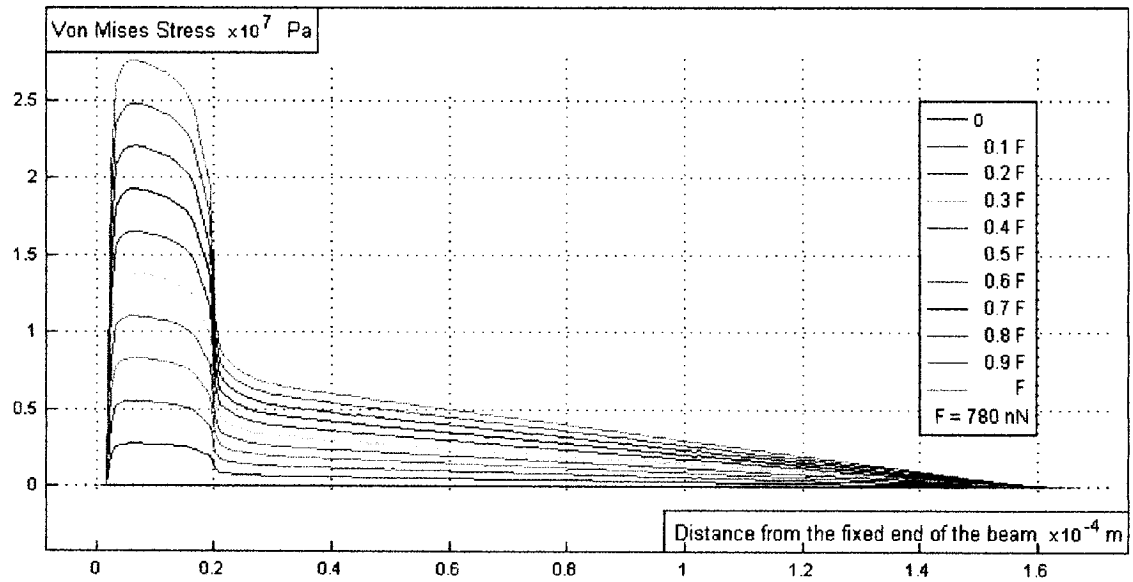

Fig.B.10. Stress distribution along the axis of one branch of the sensor.

As can be seen in this figure (which is derived along the axial line of the first branch of the resistor) the concentration of stress is between $2.5\mu m < x < 17.5\mu m$, where the resistor is located.

Eigenfrequency Analysis

Eigenfrequency analysis of Probe-1 reveals that the first eigenfrequency of the system is $42562Hz$ and the second one is $2.77 \times 10^5 Hz$.

Distribution of current density

Fig.B.11 shows the distribution of current density streamlines in a top view cross section of a part of the sensor. Perpendicularity of stress and current directions that is a common drawback of meander-like strain gauges, as well as the uneven distribution of the current through the transverse parts of the sensor is shown clearly.

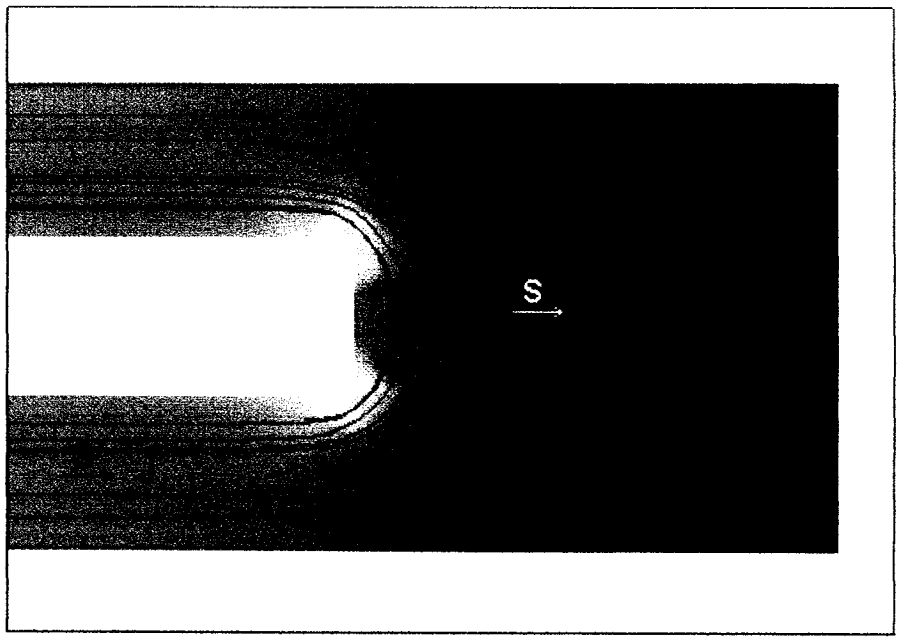

Fig.B.11. Perpendicularity of stress and current directions, and the uneven distribution of the current through the bending parts of the sensor.

The relative Change of the Resistance due to the applied force

The relative change in the value of resistance due to a force equal to $7.85\times10^{-7}N$ is measured as 7.65×10^{-4}.

Comparison

In comparison with the recommended probe structure, the fabricated test device exhibits about 10 times less sensitivity while its first eigenfrequency is almost twice as much as that of the recommended one.